http://hdl.handle.net/10552/3301

This is the **Accepted Version** of this work.

SEISMIC RESPONSE OF STEEL FIBRE REINFORCED CONCRETE BEAM-COLUMN JOINTS

* Ali A. Abbas BSc(Eng.), DIC, PhD, FHEA
School of Architecture, Computing and Engineering, University of East London,
London E16 2RD, UK
Tel.: 020 8223 6279, Fax: 020 8223 2963
E-mail: abbas@uel.ac.uk

Sharifah M. Syed Mohsin BSc(Eng.), DIC, PhD
Department of Civil and Environmental Engineering, Imperial College London,
London SW7 2BU, UK
E-mail: s.syed-mohsin08@imperial.ac.uk

Demetrios M. Cotsovos Dipl Ing, MSc, DIC, PhD, CEng
Institute of Infrastructure and Environment, School of the Built Environment, Heriot-Watt
University, Edinburgh, EH14 4AS, UK
E-mail: d.cotsovos@hw.ac.uk

* Corresponding Author.

1

ABSTRACT

The present research work aims to investigate numerically the behaviour of steel fibre reinforced concrete beam-column joints under seismic action. Both exterior and interior joint types were examined and 3D nonlinear finite element analyses were carried out using ABAQUS software. The joints were subjected to reversed-cyclic loading, combined with a constant axial force on the column representing gravity loads. The joints were initially calibrated using existing experimental data – to ascertain the validity of the numerical model used – and then parametric studies were carried out using different steel fibre ratios coupled with increased spacing of shear links. The aim was to assess the effect of introducing steel fibres into the concrete mix in order to compensate for a reduced amount of conventional transverse steel reinforcement and hence lessen congestion of the latter. This is particularly useful for joints designed to withstand seismic loading as code requirements (e.g. Eurocode 8) lead to a high amount of shear links provided to protect critical regions. The spacing between shear links was increased by 0%, 50% and 100%, whilst the fibre volume fraction (V_f) was increased by 0%, 1%, 1.5%, 2% and 2.5%. Potential enhancement to ductility, a key requirement in seismic design, was investigated as well as potential improvements to energy absorption and confinement. The work also examined key structural issues such as strength, storey drift, plastic hinges formation and cracking patterns.

2

1. INTRODUCTION

The structural analysis of frames is commonly based on the assumption that the joints formed at the beam-column intersections behave as rigid bodies. However, published experimental data [1-8] and numerical studies [9] reveal that for the case of reinforced-concrete (RC) structures, the "rigid joint" assumption is rather crude since cracks may form within the joint region early in the loading process. The behaviour of the RC joints departs even more form the rigid-joint assumption when considering the slippage of reinforcement, which may sometimes play an important role in the response of joints, especially with insufficient anchorage reinforcement length [10, 11]. As a result, the displacements and rotations transferred through each joint to the ends of the adjoining beams and columns can be significantly affected by the cracking and the ensuing deformation of the joint itself. This, in turn, may have a significant impact on the distribution of the internal actions developing along the structural elements of the frame affecting the overall structural performance. Although, current codes of practice for earthquake-resistant design require structures to comply with specific performance requirements, the effect of crack-formation within the joint region is essentially ignored during the structural analysis phase of RC frame structures. In order to safeguard against brittle types of failure and to enhance ductility and load-carrying capacity, current codes of practice, e.g. Eurocode 2 [12] and Eurocode 8 [13], dictate the use of dense arrangements of shear links especially in the critical regions of RC frames (i.e. beams, columns and within the joints). Nevertheless, this can result in reinforcement congestion which causes difficulties during concreting (i.e. incomplete compaction of concrete) and increases construction costs. Furthermore, published test data [1-8] and in particular the two studies by Tsonos [5, 6] demonstrated that design codes' provisions [12, 13] did not safeguard against premature joint shear failure because the resulting design cannot ensure that the joint shear stress will be significantly lower than the joint ultimate strength in order to ascertain the development of the optimal (ductile) failure mechanism with plastic hinges forming in the beams while columns remained essentially elastic, to conform to the requisite "strong column-weak beam" tenet of capacity design. An improved model was also proposed in order to ensure that beam-column joints are kept intact during strong earthquakes [6].

The present research work was carried out to examine numerically the potential benefits stemming from the introduction of steel fibres into the concrete mix on the nonlinear

behaviour of RC beam-column joint assemblages under seismic action. The aim is to investigate whether the use of steel fibres can (i) improve the structural performance of the joint, (ii) enhance the overall structural response of the RC structural configurations presently studied and (iii) lead to a substantial reduction of conventional steel reinforcement (particularly shear links). The nonlinear analysis of the responses of the RC structural configurations investigated is based on the use of the well-known commercial finite element software package ABAQUS [14]. The programme is capable of carrying out three-dimensional (3D) static and dynamic nonlinear finite element analysis (NLFEA) and incorporates material models describing the nonlinear behaviour of plain concrete. The latter was modified in order to introduce the effect of steel fibres particularly on the cracking processes concrete undergoes when subjected to external loading. Based on initial phase of the present work [15-17], the adopted model was found to be capable of providing realistic predictions concerning the response of conventionally reinforced and steel fibre reinforced concrete (SFRC) beams under both monotonic and cyclic loading. The attention of the numerical investigation was initially focused on validating the predictions obtained for the nonlinear behaviour of SFRC beam-column joints selected for this study [4,18]. At the same time the present investigation also aims at assessing how certain important aspects of structural response (i.e. stiffness, load-carrying capacity, deformation profile, cracking, ductility and mode of failure) are affected by the presence of the steel fibres within the concrete medium. For this purpose two types of beam-column joint assemblages are considered herein, namely: an external (T-shape) and a series of internal (Cross-shape) joints. The behaviour of these specimens was studied experimentally in the past by Filiatrault *et al.* [4] and Bayasi and Gebman [18]. The joints were subjected to reversed-cyclic loading, which is the key feature of seismic action, combined with a constant axial force on the column representing gravity loads.

Following the validation of the numerical predictions, a parametric investigation was carried out aiming at assessing the extent to which the enhancement of concrete material properties (through the use of steel fibres) can improve the structural performance of the RC beam-column joints mentioned earlier at both the serviceability and ultimate limit states. Furthermore, the present investigation examined whether the use of steel fibres can result in a substantial reduction of conventional transverse reinforcement without compromising ductility and strength requirements set by the current design codes [12,13]. The parameters considered herein are the fibre volume fraction (V_f) and the spacing increase (SI) between

4

the shear links. The spacing between shear links was increased while steel fibres were added as a substitute (so the spacing between shear links was increased by 0%, 50% and 100%, while the fibre volume fraction (V_f) was increased by 0%, 1%, 1.5%, 2% and 2.5%). In this manner, overall conclusions were made on the potential of fibres to compensate for reduction in conventional transverse reinforcement.

2. FE MODELLING OF SFRC BEHAVIOUR

The effect of steel fibres on the behaviour of structural concrete at the material level has been investigated experimentally in the past by many researchers and an extended literature review on the subject is provided by Syed Mohsin [15]. SFRC prism specimens have been tested in compression, tension (either under direct tension or splitting) and bending. Based on the available test data, the introduction of steel-fibres into the concrete mix predominantly results in an enhancement to the tensile post-cracking behaviour exhibited after crack formation, allowing concrete to exhibit more ductile characteristics compared to the fully brittle behaviour exhibited by plain concrete specimens [19]. However, this profound improvement is not observed in the case of uniaxial compression. This suggests that the fibres within the concrete mix act primarily in tension, prohibiting the formation and extension of cracking, whereas in compression one could conservatively assume that their effect on the concrete strength could be ignored.

Depending on the amount and type of fibres used, the post-cracking behaviour is either described by a strain softening or hardening stress-strain branch. The residual strength exhibited after the onset of cracking is the result of the steel-fibres bridging the crack and the bond developing between the fibre and the surrounding concrete on either side of the crack. The use of small fibre contents normally results in a softening post-cracking response as the first cracking strength is the ultimate strength and further deformation is governed by the opening of a single crack. On the other hand, the addition of higher values of fibre content can result in a strain-hardening response as the fibres are able to sustain more load after the formation of the first crack and consequently more cracks will be formed (thus, this type of behaviour is associated with the formation of multiple cracks). The amount of crack opening affects the shear behaviour. Usually in the non-linear FE analysis of reinforced-concrete structures "shear retention" is used to allow for the effect of aggregate interlock and dowel action. Fibres provide a similar effect on shear response (i.e. in a direction parallel

to the crack) and, therefore, it was modelled using the "shear retention" part of ABAQUS [14] concrete model. The shear stiffness of the concrete decreases when crack is propagated. Therefore, in order to allow for degradation in shear stiffness due to crack propagation, the shear modulus was reduced in a linear fashion from full shear retention (i.e. no degradation) at the cracking strain to 50% of that value at the ultimate tensile strain.

The "brittle cracking model" in ABAQUS [14] was adopted for the present work. The model is designed for cases in which the material behaviour is dominated by tensile cracking as is normally the case for structural concrete. To make the numerical solution even more efficient, the analysis is usually carried out using the dynamic solver as a quasi-static one (i.e. with a low rate of loading). Therefore in the present study, "brittle cracking model" was used in conjunction with the explicit dynamic procedure available in ABAQUS/Explicit. This was one of the practical reasons for selecting the model for the present investigations of SFRC behaviour under reversed-cyclic loading. Moreover, the model was successfully used to predict the responses of different SFRC forms such as simply-supported beams, statically-indeterminate elements as well as the present study of joints. The studies have shown that the model is capable of predicting both brittle (i.e. shear) and ductile (i.e. bending) forms of failure, as described fully elsewhere [15, 16, 17].

A number of available constitutive models for SFRC have been identified such as those proposed by RILEM [20,21], Barros [22,23], Tlemat et al. [24], Lok and Pei [25] and Lok and Xiao [26]. The constitutive relations have been developed to describe the uniaxial tensile stress-strain relationship of SFRC (in particular the post-cracking behaviour of SFRC allowing the latter to exhibit more ductile characteristics compared to the brittle response of plain concrete [19]). In these models, the residual strength beyond the cracking point of concrete is made up of two components, the steel fibres bridging the crack and the bond developing between the fibre and the surrounding concrete (leading eventually to pull-out failure when such bond is lost under increased loading). The main characteristics of the models were closely studied and a calibration study was undertaken by Syed Mohsin [15] and Abbas et al. [16,17] using NLFEA to examine these models and it was found that the use of Lok and Xiao model [26] to simulate SFRC material behaviour in tension resulted in realistic predictions concerning the response of a wide range of structural forms. Consequently, this model was selected for the subsequent parametric studies. In the model, the post-cracking behaviour of SFRC is described by the tension softening (and in some cases hardening) portion of the

stress-strain curve exhibited after crack formation, which is dependent on the fibre content as well as the shape and size of the fibres. The stress-strain relationships describing the behaviour of SFRC under uniaxial tension are:

$$\sigma = f_t\,[2(\varepsilon/\varepsilon_{to}) - (\varepsilon/\varepsilon_{to})^2] \qquad \text{for } (0 \le \varepsilon \le \varepsilon_{to})$$

$$\sigma = f_t\,[1 - (1 - f_{tu}/f_t)(\varepsilon - \varepsilon_{to}/\varepsilon_{t1} - \varepsilon_{to})] \quad \text{for } (\varepsilon_{to} \le \varepsilon \le \varepsilon_{t1}) \qquad (1)$$

$$\sigma = f_{tu} \qquad \text{for } (\varepsilon_{t1} \le \varepsilon \le \varepsilon_{tu})$$

where f_t, f_{tu} are the ultimate and residual tensile strengths of SFRC whereas, ε_{to} and ε_{t1} are the corresponding strains defined as [25]:

$$f_{tu} = \eta.V_f.\tau_d.L/d \qquad , \qquad \varepsilon_{t1} = \tau_d.L/d.1/E_S \qquad (2)$$

where η is the fibre orientation factor that takes account of the 3 dimensional (3D) random distribution of fibres, which takes values between 0.405 to 0.5 [26]. In addition, V_f is the fibre volume fraction, τd is the bond stress between concrete and steel fibres, L/d is the aspect ratio of the steel fibre and E_s is the modulus of elasticity of steel fibres.

The cracking process that concrete undergoes is modelled by employing the smeared crack approach. A crack forms when the predicted value of stress developing in a given part of the structure corresponds to a point in the principal stress space that lies outside the surface defining the failure criterion for concrete, thus resulting in localised material failure. The plane of the crack is normal to the direction in which the largest principal tensile stress acts. For purposes of crack detection, a simple Rankine failure criterion is used to detect crack initiation (i.e. a crack forms when the maximum principal tensile stress attains the specified tensile strength of concrete). The concrete medium is modelled by using a dense mesh of 8-node brick elements; the element formulation adopts a reduced integration scheme. The concrete model adopts fixed, orthogonal cracks, with the maximum number of cracks at a material point limited by the number of direct stress components present at that material (Gauss) point of the finite element model (a maximum of three cracks in three-dimensional). Allowance is made for crack closure, which is important in simulating cyclic loading. An iterative procedure based on the well-established Newton-Raphson method is used in order to account for the stress redistributions during which the crack formation and closure checks as well as convergence checks are carried out. The iterations are repeated until the residual forces attain a predefined minimum value (i.e. convergence criteria).

In the present study, the steel properties for longitudinal bars and shear links were modelled using a standard elastic-plastic material model. The stress-strain relation adopted is the one recommended in Eurocode 2 [12], which employs isotropic hardening in which the yields stress increases as plastic straining occurs. An ultimate tensile strain was also defined to detect any failure on the steel main bars or stirrups. The reinforcement bars (both longitudinal and transverse) were simply modelled as 1D truss elements, which is realistic since they have no practical flexural stiffness.

3. STRUCTURAL FORMS INVESTIGATED

Two types of beam-column joint assemblages were considered in the present investigation, an external (T-shape) and a series of internal (Cross-shape) joints. The response of the external joints was established experimentally by Bayasi and Gebman [18] whereas the response of the internal joints was established by Filiatrault *et al.* [4].

3.1. External joints specimens

The geometry and reinforcement arrangements for the external beam-column joint [18] are presented in Fig. 1. Hooked-end steel fibres, 30 mm in length, 0.5 mm in diameter were added to the concrete mix in order to achieve a fibre content of V_f = 2% (expressed as a volume fraction). The hoops (i.e. stirrups) spacing considered is 152 mm centre-to-centre uniformly applied throughout the beam and column. The uniaxial compressive (f_c) and tensile (f_t) strength of concrete was 23.9MPa and 2.4MPa, respectively. The yield stress (f_y) and the modulus of elasticity (E_s) of both the longitudinal and transverse reinforcement bars was 420 MPa and 206 GPa, respectively. The stress-strain diagram describing the behaviour of SFRC in uniaxial tension is depicted in Fig. 2a. The stress-stain curve describing the behaviour of the (longitudinal and transverse) reinforcement bars in tension and compression is shown in Fig. 2b. During testing the top and bottom of the column were restrained so as to form hinges and reversed-cyclic loading was applied vertically in the form of a concentrated displacement load near the free-end of the cantilever beam (see Fig. 1). The loading history input data adopted in this case study is shown in Fig. 3. Steel plates of 20 mm thickness were added at the support for the whole surface area of the column, and at loading point region along the beam width (this is to mimic experimental conditions and also avoid development of stress concentrations and premature localised failure in the FE simulation).

3.2. Internal joint specimens

The geometry and reinforcement details of the three full-scale internal beam-column joints (specimens S1, S2 and S3) tested by Filiatrault *et al.* [4] are presented in Fig.4. The specimens were arranged to have the same the longitudinal reinforcement in the beam and column and to differ only in the transverse (i.e. shear links) arrangements. The idea was that one specimen would have full conventional seismic shear reinforcement, while the other two would have reduced conventional reinforcement with fibres being added as a replacement in one specimen and with no fibres in the other. Therefore, one of the joints specimens S2 (see Fig. 4b) was designed with seismic detailing in accordance to the National Building Code of Canada [27] and thus was provided with a dense arrangement of (double) shear links. This is similar to the seismic detailing required to protect the critical regions recommended by the European codes [13].

The other two joint specimens S1 and S3 (shown in Fig. 4a) were provided with less shear links than S2 and therefore do not satisfy the code seismic provisions. No steel fibres were used for specimen S1, whereas in the case of specimen S3 hooked-end steel fibres were introduced in the critical region around the joint with V_f = 1.6% (i.e. the SFRC zone on specimen S3 covers the range occupied by the closely-spaced shear links in Figure 4b). Thus joint S1 represents the specimen with deficient seismic reinforcement, while S3 represents the SFRC joint with fibres added to compensate for the reduced conventional seismic reinforcement. The hooked-end steel fibres had a length of 50 mm and a diameter of 0.5 mm. The compressive strength f_c and elasticity modulus E_c of plain concrete as well as the yield strength f_y of the steel reinforcement bars was 46 MPa, 35GPa and 400 MPa, respectively. The stress-strain diagrams describing the behaviour of plain and steel fibre reinforced concrete in tension are depicted in Fig. 5a. The stress-stain diagram describing the behaviour of the reinforcement bars (both longitudinal and transverse) in tension and compression is shown in Fig. 5b.

During testing both ends of the column were assumed to be simply supported in order to simulate mid-storey inflection points (with a roller at the top to allow the application of the axial load), while the beam has free ends. A constant axial compressive load of 670 kN was initially imposed onto the column representing 100% gravity load of the 2nd floor of the central column of the prototype building. Subsequently the specimen was subjected to a reversed-cyclic loading (presented in Fig. 6) applied using a displacement-controlled

procedure through an arrangement of hydraulic actuators at specific locations along the span of the beams as shown in Fig. 7. Based on Fig.7, the storey shear (V_{col}) and storey drift (Δ_{col}) can be calculated based on the following simple expressions: $V_{col}=(P_1l_1+ P_2l_2)/ l_{col}$ and $\Delta_{col}=(\Delta_{B1}+\Delta_{B2})/(l_1+ l_2)l_{col}$, respectively. In the preceding equations, P_1 and P_2 are the actuator forces, l_1 and l_2 are the distances of vertical actuators from the joint centre, Δ_{B1} and Δ_{B2} are the vertical displacements at the loading points and l_{col} is the total column height between supports (see Fig. 7).

4. FE MODELLING OF JOINT SPECIMENS

The concrete medium is modelled with a dense mesh of 8-node brick finite elements (Fig. 8). Based on a sensitivity analysis carried out on reinforced concrete and SFRC beams [15], the optimum dimension of the brick elements was determined to be 50 mm. The optimum mesh size was determined based on calibration with existing experimental data (i.e. this is the mesh which best reproduce experimental data). Reinforcement bars were modelled by 2-noded single Gauss point truss elements and were located to match the detailing of reinforcement used in the specimens (e.g. spacing between bars, cover distance ..etc). The boundary conditions in the FE model of Fig. 8 also mimic the experimental ones. As mentioned earlier, rigid elements (similar in shape and size to the steel platens used in the experiment) were used at the supports and at the points of loading in order to better distribute the stressed developing by the applied concentrated loads and reactions and to avoid pre-mature localised cracking which can cause numerical instability. Furthermore, in order to streamline the definition of the cyclic loads applied on the beams in the FE model, the loading arrangement from the experimental work was simplified by assuming that the distances of vertical actuators from the joint centre are equal, i.e. $l_1 = l_2$ (refer to Fig. 7). Therefore, it can be considered that $\Delta_{B1} = \Delta_{B2}$. Thus, the distance adopted in the FE analysis was taken as the average of the two lengths considered in the experimental work. The effect on the results is negligible as the loads are sufficiently far from the joints and surrounding zone, which was the area of interest in terms of results.

5.   COMPARATIVE STUDIES WITH EXPERIMENTAL DATA

5.1. Exterior beam-column joint

Fig. 9 shows the load-deflection hysteresis loops based on both the numerical predictions and the corresponding experimental data [18] concerning the response of the external joints depicted earlier in Fig. 1. The results describe the relationship between the reversed-cyclic load (applied at the edge of the cantilever beam) and the vertical deflection at the same point. The key characteristics of the curves are also summarised in a tabular from underneath the figure. The key structural parameters summarised in the tables are the yield load (P_y) and corresponding deflection (δ_y), the maximum load sustained during the loading cycles (P_{max}) and corresponding deflection (δ_{max}), the load at failure (P_u) and corresponding deflection (δ_u)u and the ductility ratio (μ) defined as $\mu = \delta_u/\delta_y$. The comparison between the experiment data and numerical predictions shows good agreement. However, the highest ductility predicted by the FE analysis is about half the maximum ductility achieved in the experiment. This is due to the difference in the number of cycles obtained (i.e. ~ 4 cycles in the FE analysis compared to 5 in the experiment). So the ductility levels were the same for the first 4 cycles, however the presence of the 5th cycle in the experimental data led to this discrepancy (with the FE predictions being on the safe side). During the numerical investigation, failure (i.e. loss of load carrying capacity) was associated with an abrupt large increase in kinetic energy as shown in Fig. 10, indicating the presence of large/extensive cracks within and around the joint region.

5.2. Interior beam-column joint

Figures 11 a, b and c show a comparison between the FE-based hysteresis curves – describing the relationship between the storey shear and storey drift of the internal joints shown in Fig. 4 – and their experimental counterparts [4] for the case of specimens S1, S2 and S3, respectively. Key values from the curves are summarised in a tabular from underneath the figures. As in the previous case study, the comparison of the experimental data and numerical predictions shows good agreement. Based on the results provided in Figs 11 a to c, it is evident that the numerically predicted values of storey shear (V_y) associated with yielding and the maximum storey shear (V_{max}) associated with the ultimate load-carrying capacity are close to their experimental counterparts with a discrepancy of less than ~4%. Failure, however, occurs earlier during the numerical investigation, with the beam-column joint assemblages exhibiting deformation of up to 20% lower than that

predicted experimentally. At this point it is important to draw a distinction between the definitions of numerical failure and its experimental counterpart. During testing the loading procedure ended after the specimen suffered severe destruction of concrete within and around the joint region. On the other hand, numerical failure is considered to occur when the structure's stiffness matrix becomes non-positive or when an abrupt increase in kinetic energy is observed (similar to that of Fig. 10) due to excessive cracking within and around the joint region. During testing however, in spite the destruction of concrete, the real structure may have still been capable of sustaining the induced excitation, by resorting briefly to alternative resistance mechanisms, such as, for example, dowel action. This stage of behaviour, which clearly is neither stable nor sustainable and as such of no real significance for design purposes, is not described analytically, as the development of alternative resistance mechanisms such as the above are not accounted for by the numerical model. Nevertheless, the numerical model clearly serves the purpose of predicting, with sufficient accuracy, the maximum load and displacement values attained and any differences with their experimental counterparts are well within the accepted range of accuracy for concrete structures, with the numerical predictions being more conservative.

Figs 12 a to c show a comparison of the experimentally established crack patterns exhibited by specimens S1, S2 and S3 prior to failure with their numerical counterparts presented in the form of principal strain contours. Areas of the specimens exhibiting values of principal strain exceeding the ultimate tensile (positive) strength of SFRC of 0.02 – associated with pull-out failure - (see point D in Fig. 5) are highlighted in grey. Areas of the specimens exhibiting values of principal strain less than the ultimate compressive (negative) strain of concrete (-0.0035) are highlighted in black. From Fig. 12a, specimen S1 (i.e. with $V_f = 0$ and shear links that do not satisfy seismic code specifications) failed due to extensive cracking within the joint region. Specimen S2 (i.e. with $V_f = 0$ and shear links that satisfy seismic code specifications), on the other hand, failed after the formation of plastic hinges – see grey regions in Fig. 12b – at the support of the beams of joint assemblage. This indicates that plastic hinges develop at the roots of the beams adjoining the columns as intended in the design. Cracking within the joint region was reduced compared to that exhibited in specimen S1. Finally, the mode of failure of specimen S3 (i.e. the one with $V_f > 0$ and shear links that do not satisfy code specifications) was similar to the mode of failure exhibited by specimen S2 indicating that the introduction of steel fibres compensate to a large extent for the insufficient shear links. As in the case of specimen S2, plastics hinges (see grey regions in Fig.

12c) form at the ends of the beams. This is a key requirement in seismic design (i.e. capacity design concept utilising strong column–weak beam philosophy [13,28,29]. Furthermore, the compressive strains were lower than 0.0035 suggesting that no crushing failure has occurred.

6. PARAMETRIC STUDIES ON EXTERNAL BEAM-COLUMN JOINTS

Following the validation of the numerical predictions, parametric studies were carried out using NLFEA to examine the potential of steel fibres to compensate for reduction in conventional shear reinforcement. To achieve this, the spacing between shear links was increased, whilst steel fibres were added. Therefore, the spacing between the links was increased by SI = 0%, 50% and 100%; whilst the fibre volume fraction was increased with V_f = 0%, 1%, 1.5%, 2% and 2.5%. To account for the different fibre contents, the tensile stress-strain diagrams for both plain and SFRC adopted are presented in Fig. 13. It is interesting to note that strain-hardening occurs with high fibre contents such as V_f = 2.0% and 2.5%. It must be pointed out that the fibres do not enhance the concrete cracking stress itself, but rather the residual stress (i.e. after cracking the tensile stresses are transferred to the fibres). Further experimental evidence for the increase in residual tensile strength can be found elsewhere [30-32]. During the parametric investigations, the external beam-column joint with conventional reinforcement and no fibres (i.e. V_f = 0% and SI = 0%) was selected as the control joint specimen (CJ). The responses of all other specimen (with different fibre content and stirrup spacing) were compared to the response of the control specimen in order to establish the effect of the various parameters (i.e. fibre content and stirrup spacing) on the structural response.

6.1. Load-deflection curves

The NLFEA-based load-deflection hysteresis curves obtained for all cases investigated are presented in Figs 14a, b and c accompanied by the key values presented in tabular form. The results show that the introduction of steel fibres led to an increase of load carrying capacity and stiffness whereas the increase of the spacing of the transverse reinforcement (with SI = 50% and 100% in Figs 14b and c, respectively) resulted in a decrease of load carrying capacity and ductility. This reduction was fully or partially recovered when introducing steel fibres into the concrete mix. To study the hysteresis loops data further, comparisons were made between the control joint specimen (i.e. the one with no fibres and full conventional

shear reinforcement) and the joints with various fibre dosages and increased stirrup spacing. The values of the strength, ductility and energy absorption were normalised by dividing them by the corresponding values of the control specimen. In this manner, overall conclusions were made on the potential of fibres to compensate for reduction in conventional transverse reinforcement. The normalised values of these key structural performance indicators (under cyclic loading) also provide an estimate of the potential enhancement to these parameters and the amount of fibres required to achieve them. Such findings are useful for loading types which are characterised by their cyclic nature, such as seismic loads.

6.2. Strength

Fig. 15a shows the variation of the ratio between the load carrying capacity P_{max} of each joint considered during the parametric studies and that of the control joint specimen ($P_{max,0}$) plotted against the fibre content V_f for different spacing increases. Similarly, Fig. 15b shows the variation of the ratio between the load at yield P_y of each specimen and that of the control joint ($P_{y,0}$) plotted against V_f and SI. The graph shows that the strength consistently increases as e more fibres are added. The predictions presented in Figs 15 a, b show that increasing the stirrups spacing reduced the capacity of the conventionally-reinforced concrete joint (V_f = 0%) to sustain further loading, e.g. for joints with SI = 50%, a reduction of 18% in P_y and 11% in P_{max} compared to the control joint is observed. Similarly, for joints with SI = 100% and no fibres the decrease in P_y and P_{max} is about 28% and 59%, respectively, of their control specimen counterparts. On the other hand, adding fibres resulted in elevated values of P_y and P_{max} (e.g. increasing the fibre content for joints with SI = 0% resulted in an increase of P_y and P_{max} by up to 47% and 41% of $P_{y,0}$ and $P_{max,0}$ respectively. Similarly, for joints with SI = 50% and 100% increasing V_f resulted in elevated values of P_y (by up to 52% and 55% for joints with SI = 50% and 100%, respectively) and P_{max} (by up to 76% and 33% for joints with SI = 50% and 100%, respectively). The strength level of the control specimen was restored with fibre contents of V_f = 0.5% and 1.3% for joints with   and 100%, respectively. Higher fibre amounts led to the strength level of the control specimen been exceeded by up to 40~60%. Similarly, the yield load of joints with SI = 50% and 100% reached that of the control specimen $P_{y,0}$ when fibres were added at V_f = 1.7% and 2.2%, respectively.

6.3. Ductility

The variation of the ductility of each joint μ normalised to that of the control joint ($\mu_{,o}$) for

different values of V_f and SI is presented in Fig. 16a. The results demonstrate that that the ductility performance of the joints with increased stirrups spacing (but without fibres added to compensate) deteriorated considerably. The results also show that ductility increases as the amount of fibres is increased. The trend, however, is true up to a *critical* value (or limit) of fibre volume fraction beyond which the ductility begins to reduce. It is also interesting to note that the higher the spacing between the stirrups, the higher the critical fibre volume ratio. This suggests that the addition of fibres within an optimum range enhances ductility. However, fibres should not be provided in excessive quantities as this will lead to a stiffer response with the joint deflecting less (this is largely due to the fibres role in bridging across cracks and limiting their opening). This crack control and confinement effect is most pronounced in when fibres are provided in addition to full conventional shear reinforcement (i.e. SI = 0%). The optimum amounts of fibres were found to be approximately V_f = 1% for SFRC joints with SI = 0%, V_f = 2% for joints with SI = 50% and 100% (with   being twice that of the control specimen). For SFRC joints with SI = 50% and 10%, the ductility level of the control specimen was attained with fibres provided at V_f = 1.5%.

Therefore, it can be concluded that the addition of fibres in optimum amounts will lead to significant enhancement to ductility. This is of particular relevance to seismic design as ductility is one of the main considerations to ensure sufficient energy dissipation (energy absorption was also studied and the results are presented subsequently). Nevertheless, fibres should not be provided in excess of the optimum amounts as this will lead to a less-ductile response as mentioned earlier (the response could potentially be improved by adjusting the mix design, however this is beyond the scope of the present paper). Therefore, fibres could be provided to replace some of the conventional shear reinforcement (and thus lessen the congestion of shear links in critical regions), but should not be provided in addition to *full* conventional reinforcement.

6.4. *Energy absorption ratio*

Fig. 16b shows the variation of the energy absorbed by each joint (E_a) until failure due to nonlinear behaviour (owing to cracking of concrete and yielding of the steel bars) normalised by the energy absorption of the control joint ($E_{a,0}$) for different values of V_f and SI. The trend is similar to the one observed earlier for ductility with energy absorption increasing up to a certain peak and then dropping if excessive amounts are provided. The optimum fibre content associated with the highest levels of energy absorption were V_f = 1% for joints with

SI = 0% and V_f = 2% for joints with SI = 50% and 100%. It should be noted that the enhancement in energy absorption due to fibres is significant (with absorption levels 4~10 times higher than those associated with the control specimen).

6.5. *Principal strain contours and cracking patterns*

In order to gain better insight into how steel fibres affect the responses of the joints, attention was focussed on the distribution of principal strains which is presented in the form of contours and vectors in Figs 17 to 20 for different levels of loading. The graphs were developed to study the control joint specimen with SI = 0% at three levels of fibre content (i.e. V_f = 0%, 1% and 2%) and at different deflection points from yield to failure. The strain vectors are useful in indicating the pattern of crack formation. For presentation purposes, the upper limit value of tensile (positive) strain is set equal to 0.000239 which is associated with crack formation (i.e. Point A in Fig. 13), whereas the lower limit for compressive (negative) strain is set at -0.0035 representing the ultimate compressive strain for plain concrete. Thus the regions of the joint assemblage exhibiting tensile strains equal or larger than the above upper limit were highlighted in grey to indicate cracking zones.

The distribution of principal strains at yield (i.e. δ_y = 6.25 mm), taken at the end of the first cycle, are illustrated in Fig. 17. The contours indicate that cracking has been reduced as fibre amount provided increases. This is supported by the graphs of principal strain vectors which also show that the crack formation is less in joints with higher fibre amounts. This confirms the role of fibres in controlling crack opening. Similar conclusions are drown from Fig. 18 showing the distribution of the principal strains contours and vectors at the end of the second load cycle (δ_2 = 12.5 mm). It should be noted that in latter figures the grey area are associated with tensile strains higher than 0.001, which is the ultimate tensile strain for plain concrete (see point B_0 in Fig. 13). It can be seen that the crack formation is limited with V_f = 2% as compared to the results of specimens with less amounts of fibre.

Figure 19 shows the distribution of the principal strain contours and vectors at the end of the third cycle with a deflection δ_3 = 24.9 mm. At this level of loading (deformation) the numerical analysis predicted that the joint with fibre contents V_f = 0% and 2% suffered loss of load carrying capacity. The joint with V_f = 1% (optimum amount of fibres) was able to undertake additional loading and failed later in the loading process at the end of the forth cycle (at δ_4 = 49.9mm) and the corresponding contours and vectors are depicted in Fig. 20. It should be noted, that the regions highlighted in grey in Figs 19 and 20 are associated with

tensile strains higher than the ultimate tensile strain for SFRC of 0.02 (i.e. point D in Fig. 13) indicating pull-out failure of the fibres. The results show that increasing the values of V_f led to limited zones of pull-out failure. A similar trend of structural response to those described above is also observed for the joints with SI = 50% and 100%.

6.6. *Mode of failure*

The mode of failure of all joint assemblages considered in the present parametric studies can be observed using the principal strain contours at failure shown in Figs 21 to 23. In these graphs, the regions of the specimen highlighted in grey denote areas where the ultimate tensile strain associated with pull-out failure of 0.02 has been exceeded (i.e. point D in Fig. 13). The only exception is the joints without fibres (i.e. V_f = 0%), where the tensile strain associated with cracking of 0.001 for plain concrete is used to define the grey zone. The ultimate compressive strain of -0.0035 is adopted to indicate crushing failure and the corresponding intervals are highlighted in black. Figs 21 to 23 show that all joints with no fibres suffered extensive cracking even within the joint region prior to failure. The introduction of fibres resulted in a reduction of cracking within and around the joint region. As the fibre content was increased, the regions of the joint assemblage exhibiting pull-out failure reduced and for the majority of cases investigated the failures were limited to the beam ends, but did not extend into the column or joint region. This indicates that in SFRC joints, plastic hinges will form at the end of the beam – and not on the column – which is of particular relevance to seismic design (i.e. capacity design based on strong column-weak beam philosophy). Additionally, it was found that the extent of cracking suffered in the joint region was significantly reduced as fibres were added.

7.   PARAMETRIC STUDIES ON INTERNAL BEAM-COLUMN JOINTS

Parametric investigations, similar to those carried out for external joints, were carried out for the case of the internal joints. The internal joint specimen S2, designed in accordance to seismic code specifications with a dense arrangement of double stirrups and no fibres (i.e. V_f = 0% and *SI* = 0%), was selected as the control joint specimen. Comparing the structural response of the control joint with that of the SFRC joints with reduced conventional transverse reinforcement provided an insight into the potential for steel fibres to help lessen the congestion of stirrups. From Figs 4c,d it can be seen that both the column and beam cross-sections of the control specimen have a dense arrangement of double stirrups in order

to safeguard against shear failure and ensure an acceptable level of ductility (due to confinement). In the present study, the amount of conventional transverse reinforcement was reduced in three ways as follows:

(i)   increase in the stirrups spacing (i.e SI = 50%)

(ii)   increase in the stirrups spacing (i.e. SI = 100%)

(iii)   decrease in the hoops area from double stirrups to single stirrups in the columns (so the stirrups provided at 45° to the column sides, see Fig. 4c, were removed) but no increase in spacing

The scenarios in (ii) and (iii) above lead to the same level of reduction in transverse reinforcement, i.e. amount halved. However, the removal of the inner stirrups provided insight into the potential of fibres to compensate for the loss of confinement provided by the double-stirrup arrangement, which is an important consideration in seismic design detailing. The latter also requires the spacing between stirrups to be within certain limits to ascertain adequate confinement. Fibres provide enhancement to confinement by controlling crack opening as they bridge the cracks. The current investigation examined whether or not this confinement is sufficient to compensate for the reduced conventional hoops (either by relaxing spacing or using single stirrups). During the present parametric investigations, as the conventional transverse reinforcement was reduced, steel fibres were added to compensate with V_f = 0%, 1%, 1.5%, 2% and 2.5%. The tensile stress-strain diagrams adopted for both plain and fibrous concrete adopted are presented in Fig. 24.

7.1. Storey shear-drift curves

The storey-shear versus storey-drift hysteresis curves obtained for all cases investigated are presented in Figs 25 to 27 accompanied by a summary of the key values in tabular form. V_y and Δ_y are the storey shear and storey drift at yield, V_{max} and Δ_{max} are the maximum storey shear sustained during the loading cycles and its corresponding storey drift, V_u and Δ_u are the ultimate storey drift at failure and corresponding storey shear, μ is the ductility ratio defined as $\mu = \Delta_u/\Delta_y$. The figures show that the introduction of steel fibres generally results in an increase in ultimate load carrying capacity and stiffness. On the other hand, the reduction of the stirrups resulted in a decrease of load carrying capacity and ductility. This reduction, as discussed in detail in the following sections, is fully or partially recovered when introducing steel fibres into the concrete mix.

7.2. Strength

The curve presented in Fig. 28a shows the variation of the maximum storey shear of internal joints V_{max} normalised to that of the control joint specimen ($V_{max,0}$) for different values of fibre content and the spacing of stirrups. The predictions presented in Fig. 28a confirm the potential of fibres to safeguard and to enhance the strength of internal joints. In comparison to the strength of the control joint, V_{max} increased by up to 53% for joints with single stirrups, 43% and 58% for joints with SI = 50% and 100%, respectively. The strength level of the control specimen was restored when fibres were added at V_f = 0.5% for joints with single stirrups or with SI = 50% and at V_f = 1% for joints with SI = 100%. Further, increase of load-carrying capacity was achieved (exceeding that of the control specimen level by ~50%) with higher fibre dosages. Similarly to Fig. 28a, the curves shown in Fig. 28b present the variation of the storey shear associated with the load at yield V_y normalised to that the corresponding values for the control specimen for different values of V_f and SI. Again it is clear that fibres enhance the load at yield, with the increase in V_y being up to 10% on average.

7.3. Ductility and stiffness

Figure 29a presents the variation in ductility of the structural configurations studied in the present parametric investigations normalised by the ductility of the control specimen for different values of V_f and SI. The results show that the addition of steel fibres improves ductility up to a certain level of fibre content. Beyond this level, a further increase of the fibre content leads to a reduction of ductility. This is a finding that has been realised earlier when examining the exterior joint. For instance in the joints with single stirrups, the highest ductility increase was observed when fibres were added at V_f = 1% ~ 1.5%. Similarly, the optimum fibre contents were found to be at V_f = 1% for both joints with SI = 50% and 100%. The ductility level of the control specimen (i.e. the one with full conventional transverse reinforcement and no fibres) was restored for both joints with SI = 50% and those with single stirrups when fibres were added with V_f = 0.5% and 0.75%, respectively. However, the ductility level of the control specimen could not be restored for joints with SI = 100% even for a high value of fibre content with V_f = 2.5%. In the latter case only about 80% of the control specimen ductility level was restored. This indicates the severity of conventional steel reduction in this case where the spacing between the stirrups has been doubled. This also shows that, from a ductility viewpoint this case is worse than using single stirrups instead of double ones, as a way of reducing transverse reinforcement congestion. The double-stirrups arrangement is usually provided to enhance confinement. This demonstrates

that fibres can provide sufficient confinement to allow the use of single stirrups. On the other hand, the loss in confinement due to doubling the spacing of stirrups is too severe to be restored using fibres in the case studied.

7.4. *Energy absorption ratio*

The energy absorption capacity calculated for the interior joints E_a was normalised to the energy absorption of the control specimen ($E_{a,0}$) as presented in Fig. 29b. The optimum fibre contents coinciding with highest energy absorption levels were found to be V_f = 1.5%. for specimens with single stirrups and V_f = 1.0% for SI = 50% and 100% The energy absorption level of the control specimen was restored for all joints except those with SI = 100% This suggests that the high increase in stirrup spacing by 100% could not be fully compensated through the use of steel fibres in the present case considered.

7.5. *Principal strain contours and cracking patterns*

In order to study the structural responses further, the FE-based principal strain contours and vectors were established at deflection levels of: (i) $Δ_y$ (associated with yielding), (ii) $Δ_{max}$ (associated with maximum load carrying capacity) and (iii) $Δ_u$ (maximum deformation exhibited prior to failure) as presented in Figures 30, 31 and 32, respectively. The samples were taken for the joints with SI = 50% at varying fibre content levels, i.e. V_f = 0%, 1% and 2%. Strain vectors are also presented in the figures and they are also useful in indicating the pattern of crack formation.

The distribution of the principal strains and vectors depicted in Fig. 30 is taken at the end of the first cycle, at which point yielding occurs (i.e. $Δ_y$ = 28.6mm). In these figures the upper limit of the strains was selected to coincide with the tensile – positive – strain associated with the onset of cracking (i.e. 0.00024, see point A in Fig. 24) and the ultimate compressive – negative – strain (i.e. -0.0035). Thus, the areas highlighted in grey indicate crack initiation. It can be seen that the principal strain for the joint with no fibres was the highest amongst all, while the strain has reduced as fibre amounts were increased indicating that crack control has been provided.

Figure 31 shows the distribution of the principal strains and vectors when the specimen attain their maximum load carrying capacity (i.e. $Δ_{max}$= 69.4mm). It should be noted that the regions of the joint with V_f = 0% highlighted in grey are associated with tensile strains higher than 0.002 (ultimate tensile strain for plain concrete, see point B_0 in Fig. 24), while for SFRC

joints with V_f = 1% and 2% the grey regions indicate strain values exceeding 0.01 (approximately half the ultimate strain of SFRC). Again, it can be seen strains as well as cracking reduce with increasing values of fibre content.

The principal strain distribution at the point of failure (i.e. Δ_u = 100.2mm) is presented in Figure 32. In this case the grey region now indicates tensile strains higher than 0.02, which is the ultimate tensile strain exhibited SFRC and is associated with pull-out failure of the fibres (point D, in Figure 24). The principal strain contours and vectors indicate that the crack opening is better controlled as the fibre content is increased and that pull-out failure occurs in increasingly limited regions of the SFRC joints (compared to an extensive grey area on the joint without fibres showing that the latter experienced wider crack opening). Finally it is interesting to see that for SFRC, pull-out failure occurred in limited zones at the ends of the beams, and not on the column or joint itself, which is desirable in seismic design.

7.6. *Mode of failure*

The numerically predicted values of principal strain prior to failure presented in the form of contours for all internal joints considered in this parametric investigation are presented in Figs 33 to 35. The contours intervals were selected so that the strains exceeding the ultimate tensile strength of SFRC of 0.02 were highlighted in grey, indicating pull-out failure. Similarly, strains higher than the ultimate compressive strain of -0.0035 were highlighted in black. The contours show that pull-out failure in SFRC joints occurred in limited regions compared to the extensive grey zones on the specimens without fibres (see Figs 33a, 34a and 35a). This comparison reveals that the latter the specimens exhibited wider cracks over more extended areas. It is interesting to see that pull-out failure occurred at the ends of the beams and not within the column or joint itself. This indicates that plastic hinges formed at the ends of the beams thus satisfying the strong-column weak-beam philosophy adopted by Eurocode 8 [13] for the seismic design of RC frames.

8. DESIGN CONSIDERATIONS

An attempt was made to quantify the fibre dosage needed to replace a given amount of stirrups, yet retaining a certain level of strength and ductility (i.e. the most critical parameters for seismic design). To demonstrate the basic idea, the results of the forgoing parametric studies on external joints were reproduced in the form of contour diagrams as shown in Fig. 36. The contours depict the effect of reducing the stirrups amount (r_{sw}) whilst

increasing the fibre content V_f on the ductility ratio   and the load-carrying capacity P_{max} for the case of external joint. Similarly to current codes of practice [12,13], the stirrup content is expressed as a ratio between the stirrups area and their spacing, i.e. A_{sw}/S. Subsequently, the reduction in conventional shear reinforcement was defined as the ratio of the stirrup area and spacing normalised by the corresponding ratio of the control specimen (the latter denoted by a zero subscript), i.e. $r_{sw} = (A_{sw}/S)/(A_{sw,0}/S_{rw,0})$. On the contour plots, the control specimen results are those associated with full conventional reinforcement and no fibres, i.e. $r_{sw} = 1$ and $V_f = 0\%$.

Fig. 36a indicates that μ decreases when $V_f > 2\%$, as mentioned earlier (see Fig. 16). From the contour plots, it can also be seen that the ductility ratio associated with the control joint specimen of (i.e. $\mu = 4$) can be maintained along a line linking points $r_{sw} = 1$ and $V_f = 0\%$ at one end and $r_{sw} = 0.5$ and $V_f = 2\%$ at the other. For clarity, this is shown as a dotted line on Fig. 36a. Similarly, the P_{max} value associated with the control specimen can be maintained along a line linking points $r_{sw} = 1$ and $V_f = 0\%$ and $r_{sw} = 0.5$ and $V_f = 1.3\%$. However, for design purposes the more stringent line determined for ductility must be adopted to ensure both strength and ductility levels of the control specimen are maintained (both lines are plotted on Fig. 36b). Subsequently, a simplified design criterion was proposed and was defined by the straight line linking points $r_{sw} = 1$ and $V_f = 0\%$ and $r_{sw} = 0.5$ and $V_f = 2\%$. Thus, the proposed line can be expressed as: $V_f(\%) = 4(1 - r_{sw})$ where V_f is the volume fraction of fibres required to replace a given reduction in conventional transverse reinforcement expressed in terms of the ratio of the stirrups content r_{sw}. As stated earlier, this attempt was made mainly to demonstrate the basic principle behind the proposed design concept, nevertheless further studies on different joint types along with field calibrations are needed before any design equations can be recommended for the use of practicing engineers.

9. CONCLUSIONS

In spite of its simplicity, the proposed NLFEA model presently employed was capable of yielding realistic predictions of the response of a number of internal and external beam column joints under reversed-cyclic loading (which is the key feature of seismic action). Initially, the numerical predictions were calibrated using existing experimental data to ascertain the accuracy of the numerical results and subsequently full parametric studies were carried out to examine the potential for steel fibres to compensate for a reduction in

conventional transverse reinforcement (suggested to lessen congestion of such reinforcement, especially in seismic design). Key structural response indicators such as strength, cracking, ductility and energy absorption were studied. The results of each SFRC joint were normalised by dividing them by the corresponding values associated with the control joint specimen (i.e. the one with full conventional transverse reinforcement and no fibres). This helped formulate the following conclusions and recommendation:

- Addition of steel fibres improved the strength consistently as the amount of fibres was increased. Fibres were also effective in controlling crack propagation. Pull-out failure was found to be at the ends of the beams (and not within the columns or joint itself), which indicates that plastic hinges formed at these locations. This is desirable in earthquake-resistant design.

- The addition of fibres in *optimum* amounts led to significant enhancement to ductility. This is of particular relevance to seismic design as ductility is one of the main considerations to ensure sufficient energy dissipation (energy absorption was also studied and the results were consistent with ductility findings). Nevertheless, fibres should not be provided in excessive amounts as this will lead to a less-ductile response.

- For exterior joints, the ductility level of the control specimen was restored with fibres added at V_f = 1.5%. For interior joints, the ductility level of the control specimen was restored for both joints with single stirrups and those with *SI* = 50% when fibres were added with V_f = 1%. However, the ductility level of the control specimen could not restored for the joint with *SI* = 100%, even when fibres were provided at dosages as high as V_f = 2.5%. This indicates the severity of conventional steel reduction in this case where the spacing between the stirrups has been doubled. The double arrangement is usually used to ensure sufficient confinement is provided. Thus the results show that fibres can provide sufficient confinement to allow the use of single stirrups. However the loss in confinement due to doubling the spacing of stirrups is too severe to be restored using fibres in the case studied.

In summary, it can be concluded that steel fibres provided in optimum amounts can substitute for conventional transverse reinforcement and thus allow for a relaxation in stirrups congestion often experienced in seismic detailing of beam-column joints. A simplified design equation was also developed to determine the fibre content needed to replace a given amount of stirrups whilst retaining the same level of strength and ductility.

REFERENCES

1. Ehsani MR, Wight JK. Effect of transverse beams and slab on behaviour of reinforced concrete beam to-column connections. ACI Jnl 1985;82:188–195

2. Ehsani MR, Wight JK. Exterior reinforced concrete beam-to-column connections subjected to earthquake-type loading. ACI Jnl 1985;82:492–499

3. Tsonos AG, Tegos IA, Penelis GGR. Seismic resistance of type 2 exterior beam-column joints with inclined bars. ACI Struct Jnl 1992;89(1):3–12

4. Filiatrault A, Pineau S, Houde J. Seismic Behaviour of Steel Fiber-Reinforced Concrete Interior Beam-Column Joints. ACI Struct Jnl 1995;92(5):543–552.

5. Tsonos AG. Cyclic load behaviour of reinforced concrete beam–column subassemblages designed according to modern codes. Eur Earthq Eng 2006;3:3–21

6. Tsonos AG. Cyclic load behavior of reinforced concrete beam–column subassemblages of modern structures. ACI Struct Jnl 2007;104:468–478

7. Kotsovou G, Mouzakis H. Seismic behaviour of RC external joints, Mag Concr Res 2011;63(4):247–264.

8. Kotsovou G, Mouzakis H. Seismic design of RC external beam-column joints. Bull Earthq Eng 2012;10(2):645–677.

9. Cotsovos DM and Kotsovos MD. Cracking of rc beam / column joints: Implications for practical structural analysis and design. The Struct Eng 2008;86(12):33–39.

10. Fleury F, Reynouard JM and Merabet O. Finite element implementation of a steel-concrete bond law for nonlinear analysis of beam-column joints subjected to earthquake type loading. Struct Eng & Mech 1999;7(1):35–52.

11. Lykidis GCh and Spiliopoulos KV. 3D Solid Finite Element Analysis of Cyclically Loaded RC Structures Allowing Embedded Reinforcement Slippage. Jnl Struct Eng ASCE 2008;134:629–638.

12. EN1992-1 Eurocode 2. Design of Concrete Structures—Part 1-1. General Rules and Rules for Buildings. Brussels: European Committee for Standardization; 2004.

13. EN 1998-1 Eurocode 8. Design of Structures for Earthquake Resistance—Part 1. General Rules, Seismic Actions and Rules for Buildings. Brussels: European Committee for Standardization; 2004.

14. ABAQUS Version 6.7 Documentation; 2007. Accessed online at http://www.engine.brown.edu:2080/v6.7/index.html

15. Syed Mohsin SM. Behaviour of fibre-reinforced concrete structures under seismic loading. PhD thesis. Imperial College London; 2012.

16. Abbas AA, Syed Mohsin SM, Cotsovos DM. Numerical modelling of fibre reinforced concrete. Proceedings of the International Conference on Computing in Civil and Building Engineering icccbe 2010, Nottingham, UK (Tizani W. (ed)). University of Nottingham Press; 2010, Paper 237, p. 473, ISBN 978-1-907284-60-1.

17. Abbas AA, Syed Mohsin SM, Cotsovos DM. A comparative study on modelling approaches for fibre-reinforced concrete. Proceedings of the 9th HSTAM International Congress on Mechanics. Limassol, Cyprus, 12-14 July; 2010.

18. Bayasi Z, Gebman M. Reduction of Lateral Reinforcement in Seismic Beam-Column Connection via Application of Steel Fibres. ACI Struct Jnl 2002;99(6):772–780.

19. Kotsovos MD, Pavlovic MN. Structural concrete: Finite-element analysis for limit-state design. London: Thomas Telford; 1995.

20. RILEM Technical Committees. RILEM TC 162-TDF: Test and Design Methods for Steel Fibre-Reinforced Concrete, Recommendation: Design Method. RILEM Mater and Struct 2000;33:75–81.

21. RILEM Technical Committees. RILEM TC 162-TDF: Test and Design Methods for Steel Fibre-Reinforced Concrete, Final Recommendation: Design Method. RILEM Mater and Struct 2003;36:560–567.

22. Barros JAO, Figueiras JA. Flexural behavior of SFRC: Testing and modelling. Jnl Mater in Civ Eng ASCE 1999;11(4):331–339.

23. Barros, JAO, Figueiras JA. Model for the Analysis of Steel Fibre Reinforced Concrete Slabs on Grade. Comput and Struct 2001;79(1):97–106.

24. Tlemat H, Pilakoutas K, Neocleous K. Modelling of SFRC using Inverse Finite Element Analysis. RILEM Mater and Struct 2006;39:221–233.

25. Lok TS, Pei JS. Flexural Behavior of Steel Fiber-Reinforced Concrete. Jnl Mater in Civ Eng ASCE 1998;10(2):86–97.

26. Lok TS, Xiao JR. Flexural Strength Assessment of Steel Fiber-Reinforced Concrete. Jnl Mater in Civ Eng ASCE 1999;11(3):188–196.

27. NRCC. National Building Code of Canada, Associate Committee on the National Building Code, National Research Council of Canada, Ottawa, ON; 1990.

28. Booth E, Key D. Earthquake Design Practice for Buildings. 2nd ed. London: Thomas Telford; 2006.

29. Elghazouli AY. Seismic Design of Buildings to Eurocode 8. Oxon: Spon Press; 2009.

30. Lim DH and Oh BH. Experimental and theoretical investigation on the shear of steel fibre reinforced concrete beams. Eng Struct 1999;21(10):937–944.

31. Yazici S, Inan G and Tabak V. Effect of aspect ratio and volume fraction of steel fiber on the mechanical properties of SFRC. Construct and Build Mater2007;21(6):1250–1253.

32. Chalioris CE and Karayannis CG. Effectiveness of the use of steel fibres on the torsional behaviour of flanged concrete beams. Cement and Conc Compos2009;31(5):331–341.
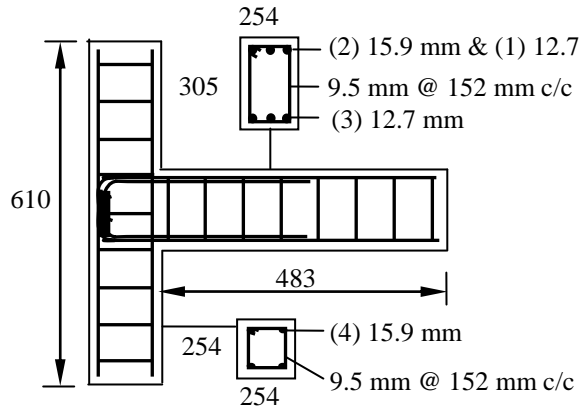
Figure 1: Geometry and reinforcement details for the external (T-shape) beam-column joint tested by Bayasi and Gebman [18] – all dimensions are in mm
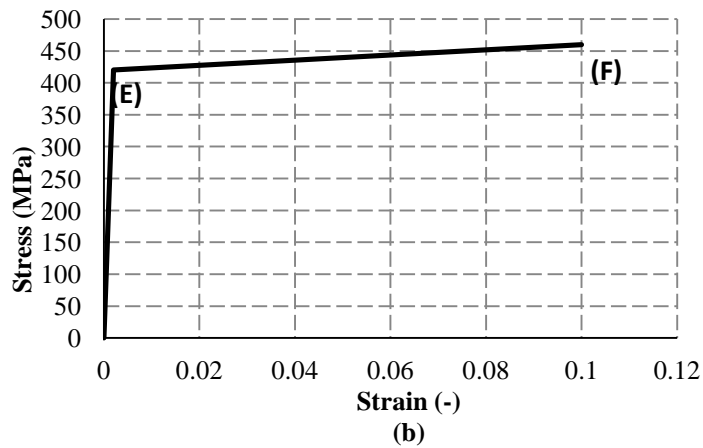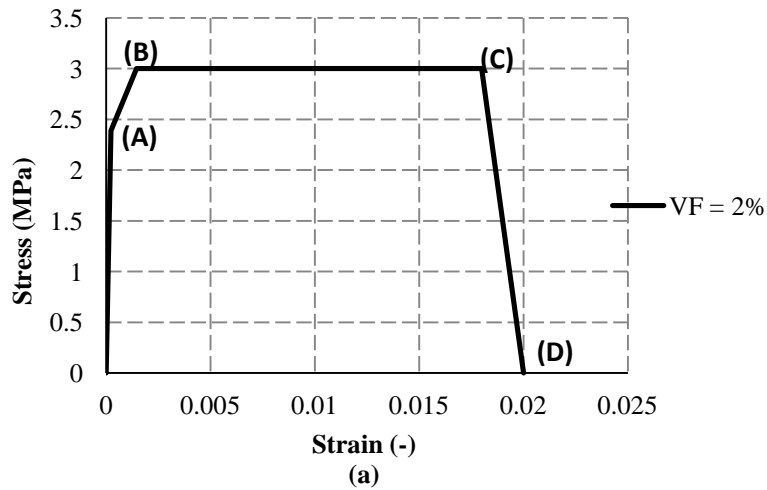
Figure 2: Stress-stain diagram for (a) SFRC and (b) conventional steel reinforcement bars adopted for the numerical modeling of the external joint experiments
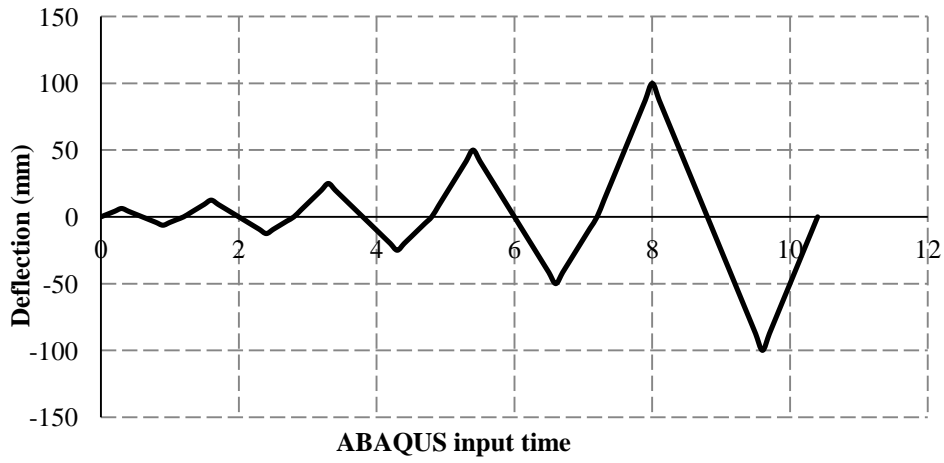
Figure 3: Reversed-cyclic loading history applied to external beam-column joints
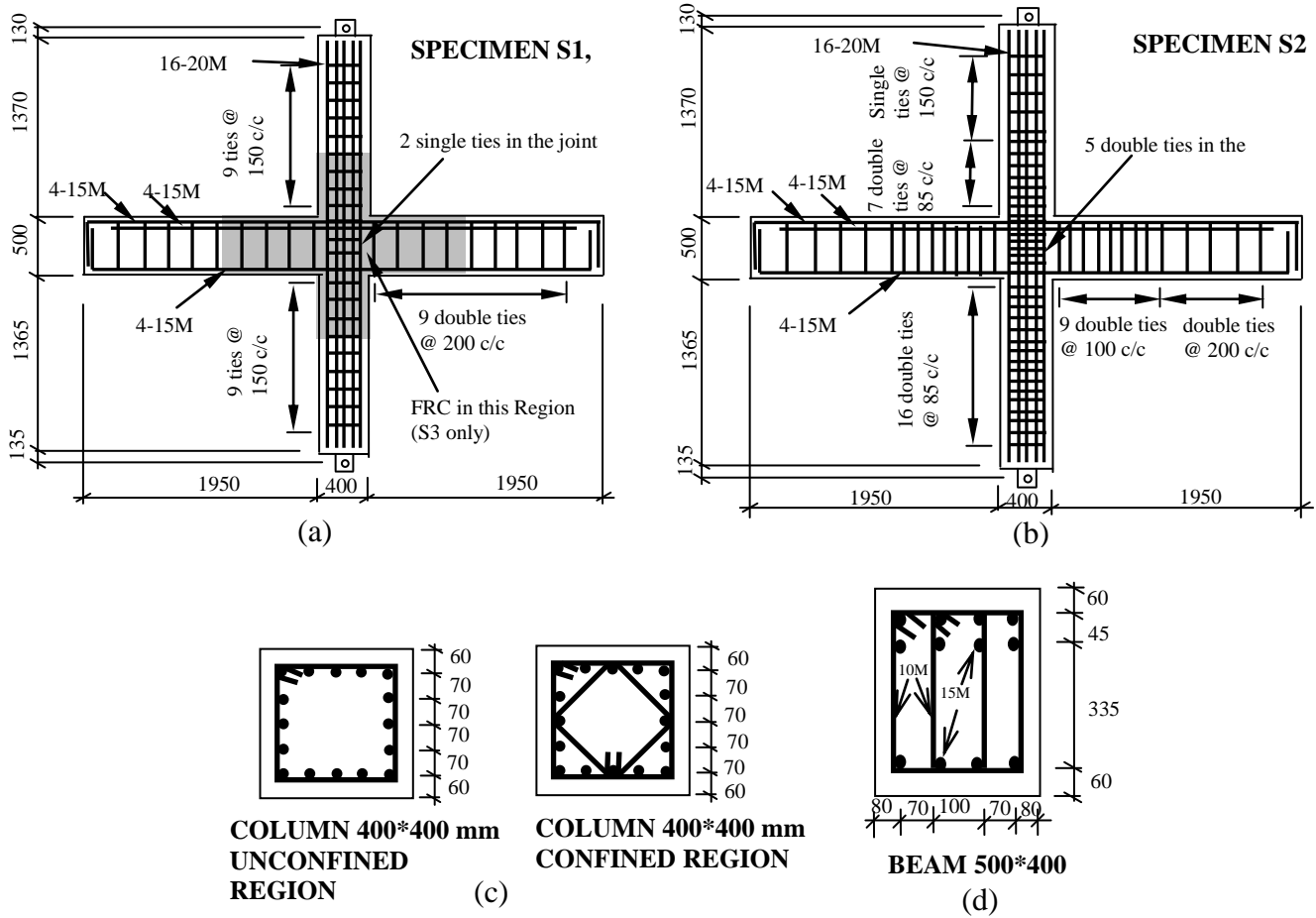
Figure 4: Details of (a) specimens S1 and S3, (b) specimen S2, (c) column cross-section and d) beam cross-section tested by Filiatrault *et al.* [4] – all dimensions are in mm
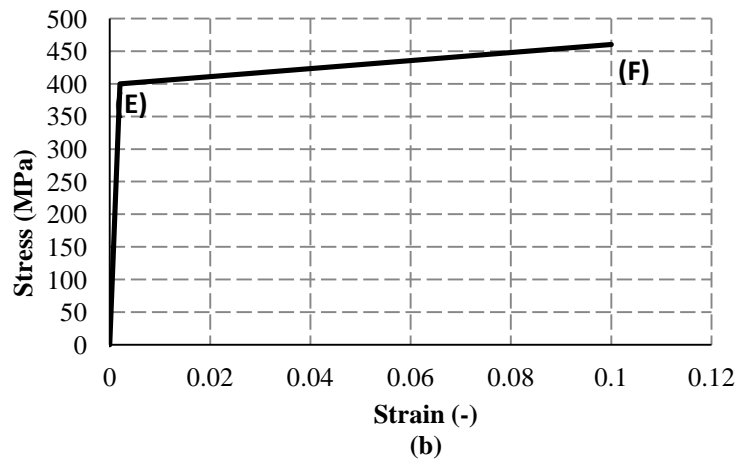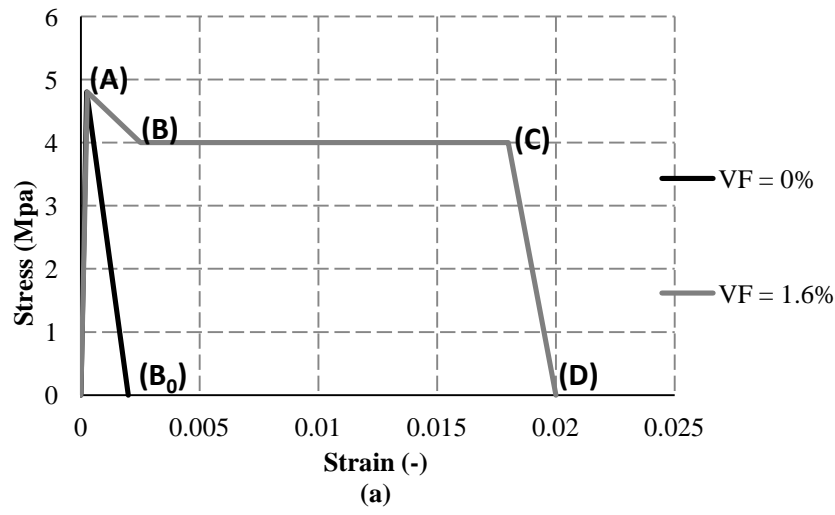
Figure 5: Stress-stain diagram for (a) plain and fibrous concrete and (b) conventional steel reinforcement bars adopted for modeling the internal joints experiments
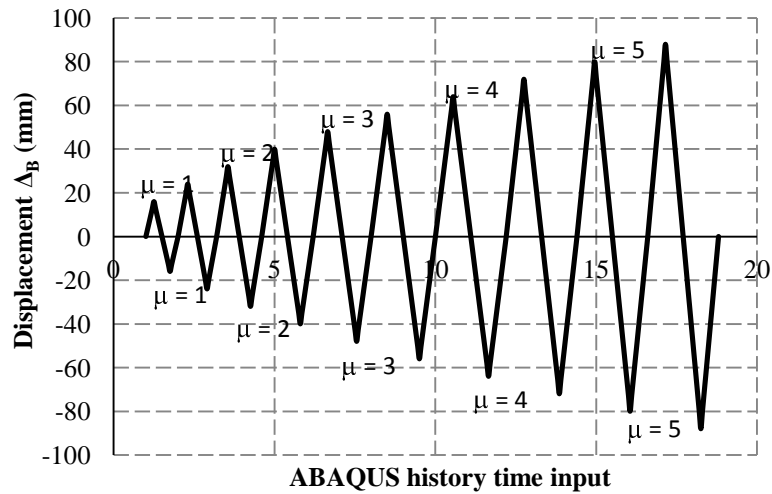
Figure 6: Reversed-cyclic loading history adopted for internal beam-column joints
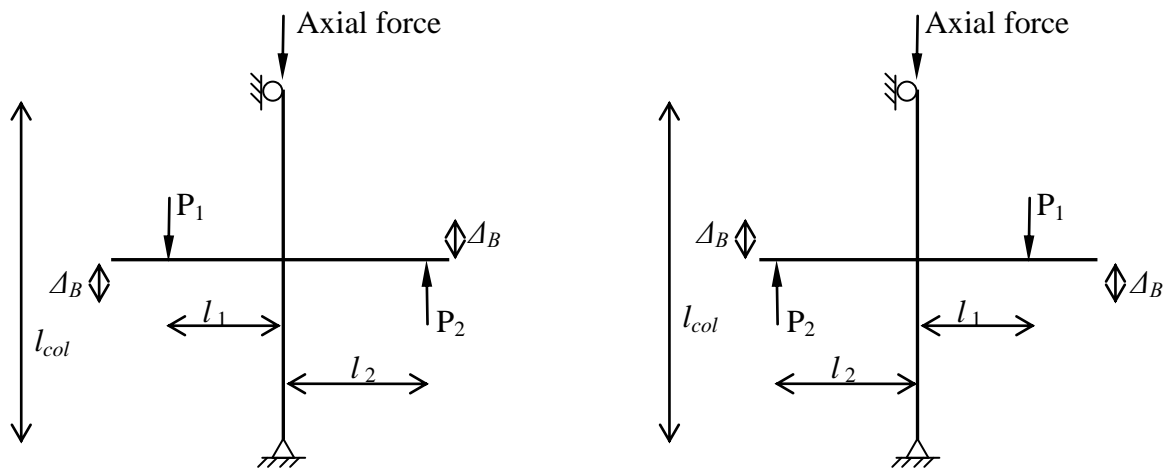
Figure 7: Loading arrangement of cyclic (left) and reversed-cyclic (right) loading used for the internal beam-column joint
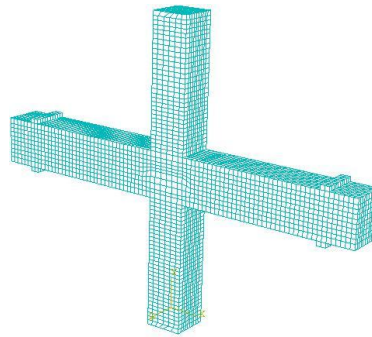
Figure 8: FE mesh adopted for modeling internal beam-column joints
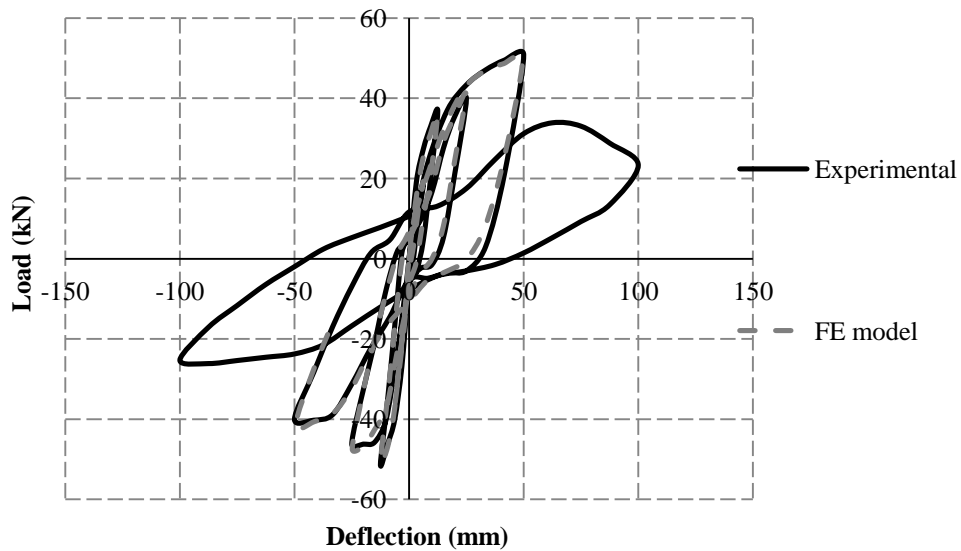
Beam-column joint	P_y (kN)	δ_y (mm)	P_u (kN)	δ_u (mm)	P_{max} (kN)	δ_{Pmax} (mm)	$\mu = \delta_u/\delta_y$	P_{max}/P_y
Experimental	18.5	6.25	23.3	100	50.9	50	16.0	2.75
FE model	19.3	6.25	50.0	49.6	50.0	49.6	7.94	2.59

Figure 9: Load-deflection hysteresis curves for external joints showing both numerical and experimental results
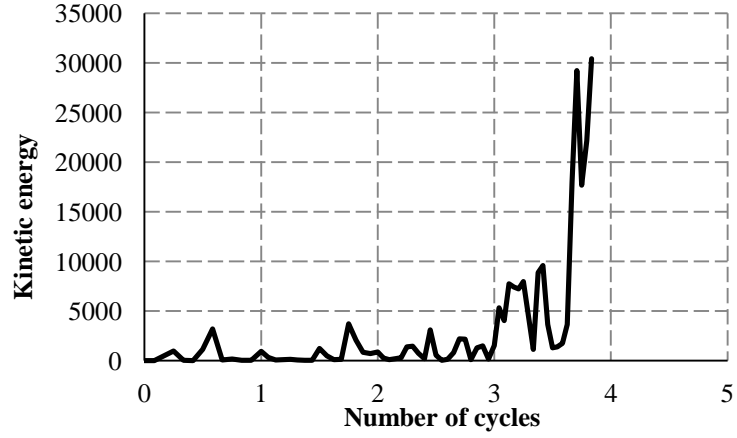
Figure 10:   Kinetic energy variation during loading of the external joint
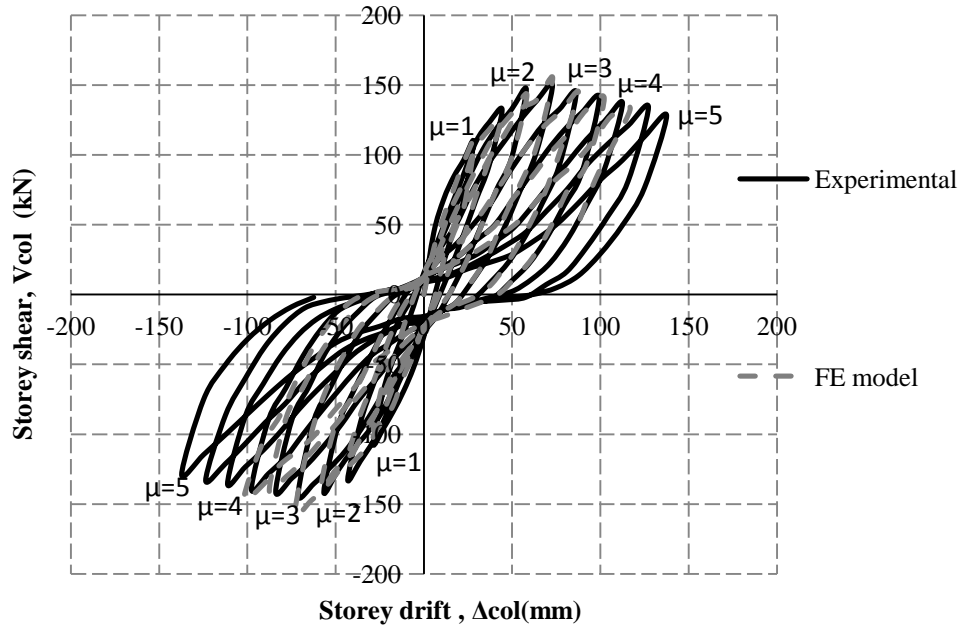
	V_f (%)	V_y (kN)	$Δ_y$ (mm)	V_{max} (kN)	$Δ_{Vmax}$ (mm)	V_u (kN)	$Δ_u$ (mm)	$μ = Δ_u/Δ_y$	V_{max}/V_y
Experiment	109.4	28.2	149.8	72.9	127.9	137.6	4.88	1.37
FE model	109.3	28.6	154.9	73.0	132.1	116.8	4.08	1.42

(a)

31
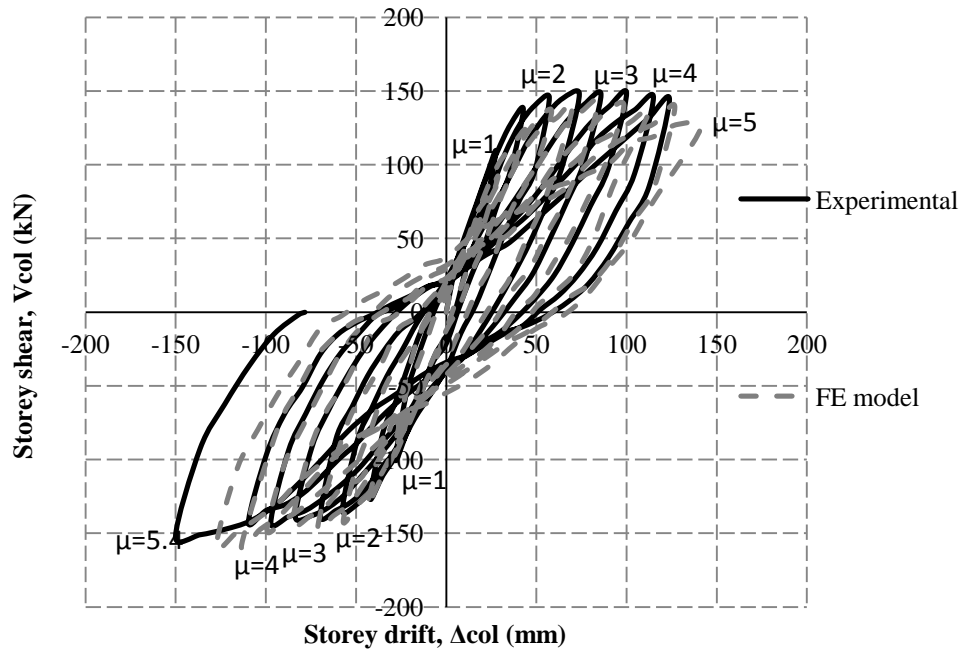
	V_f	V_y	Δ_y	V_{max}	Δ_{Vmax}	V_u	Δ_u	$\mu = $	$V_{max}/$
	(%)	(kN)	(mm)	(kN)	(mm)	(kN)	(mm)	Δ_u/Δ_y	V_y
Experiment		109.4	27.6	148	73.8	144.3	123.8	4.49	1.35
FE model		92.4	28.8	143.1	84.3	124.2	140.8	4.9	1.55

(b)
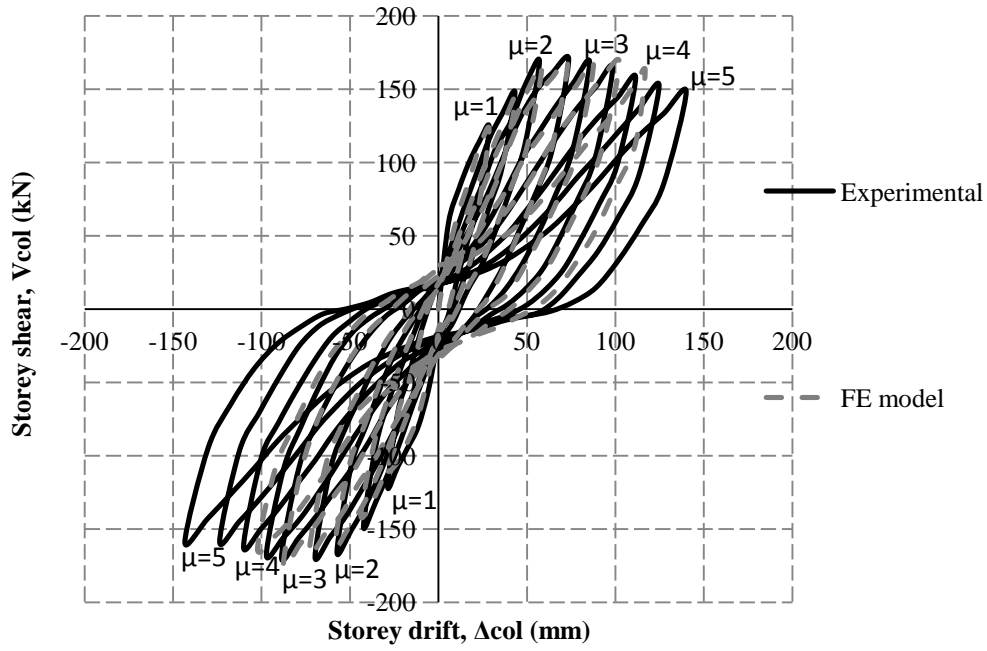
	V_f	V_y	Δ_y	V_{max}	Δ_{Vmax}	V_u	Δ_u	$\mu = $	$V_{max}/$
	(%)	(kN)	(mm)	(kN)	(mm)	(kN)	(mm)	Δ_u/Δ_y	V_y
Experiment		123.9	28.7	170.1	73.6	140.0	147.9	5.15	1.37
FE model		122.4	28.6	168.0	102.2	162.7	116.8	4.08	1.37

(c)

Figure 11:   Numerical and experimental results of storey shear-storey drift curves for internal joints (a) S1, (b) S2 and (c) S3
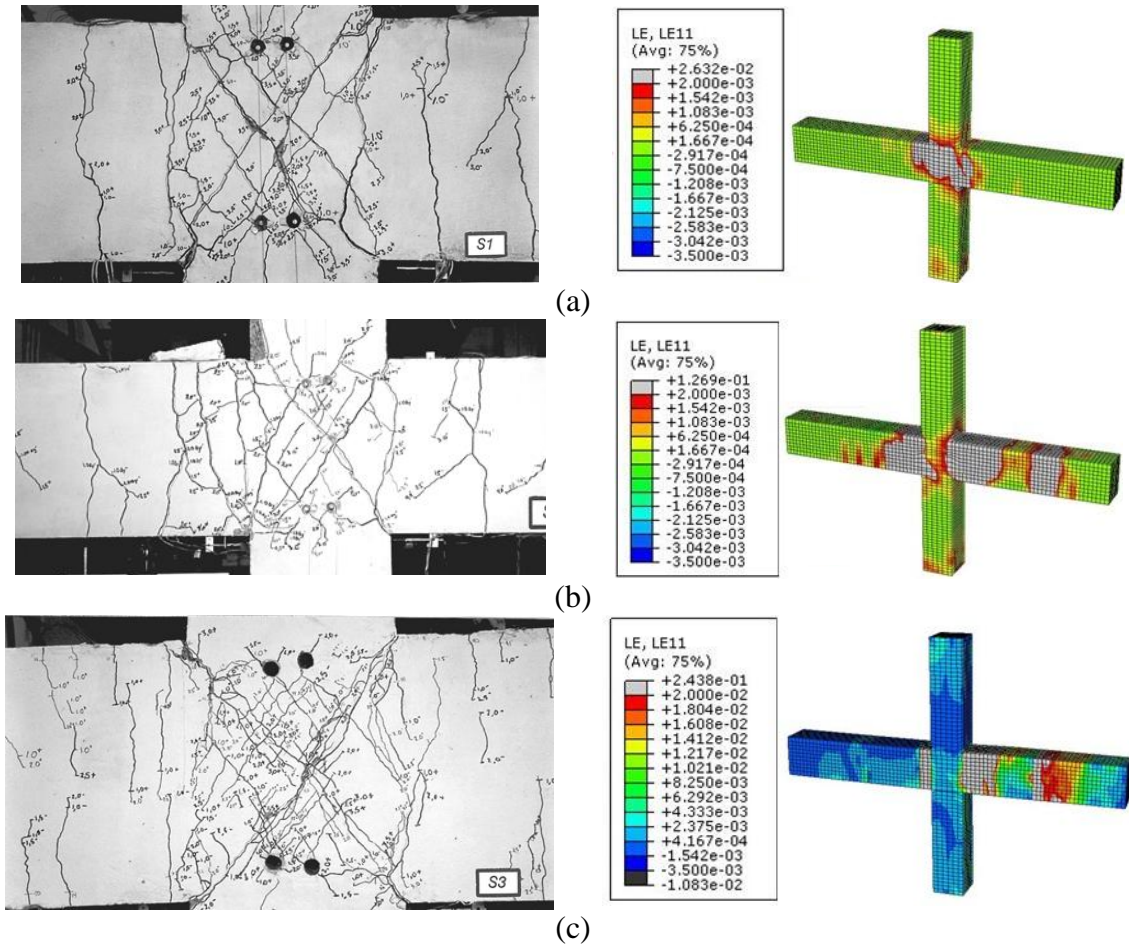
Figure 12: Comparison of experimentally established and numerically predicted crack patterns exhibited prior to failure for internal joints (a) S1, (b) S2 and (c) S3
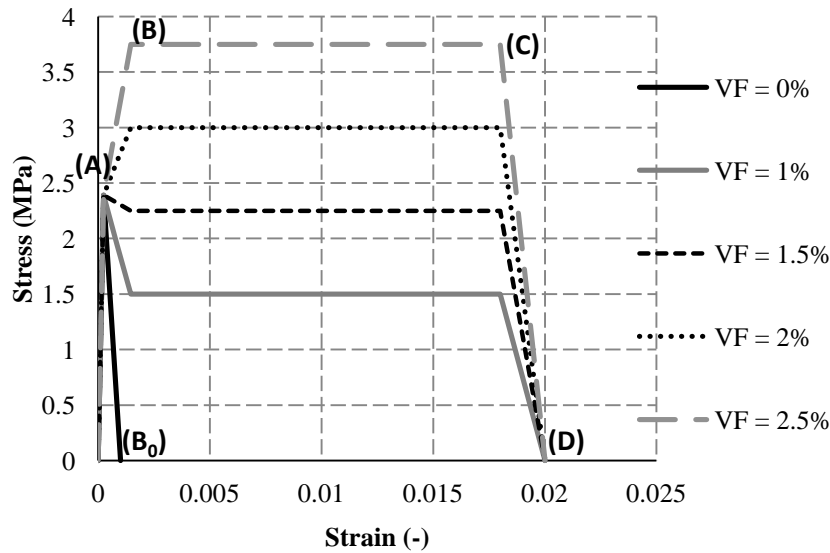
Figure 13: SFRC tensile stress-strain diagrams adopted for the parametric studies on external (T-shape) beam-column joints

33
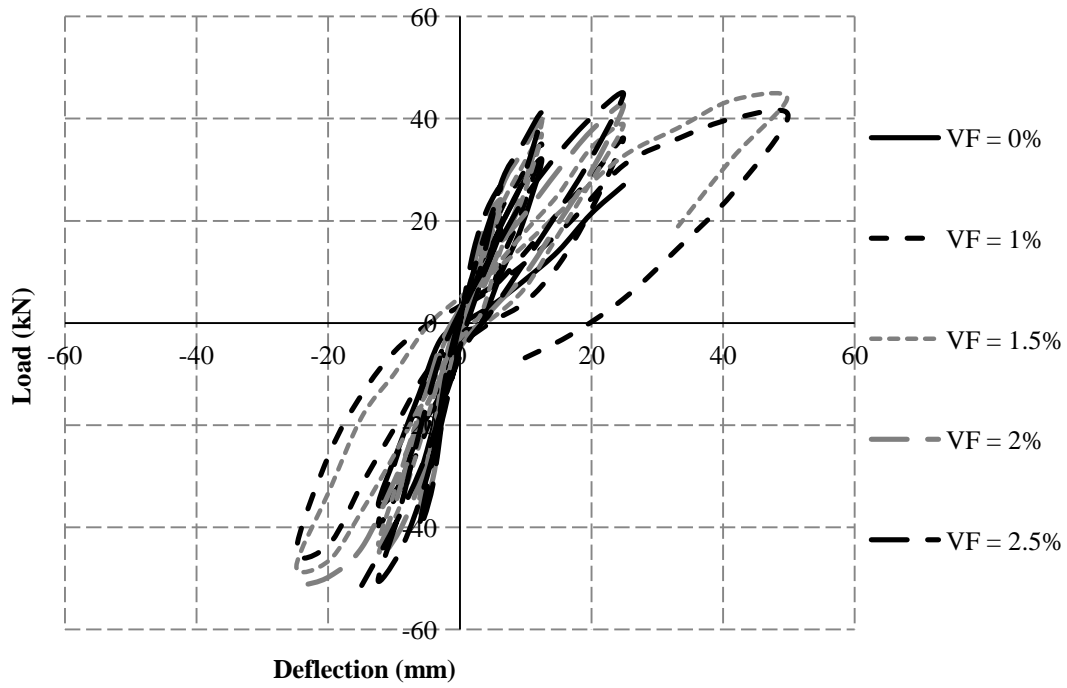
V_f	P_y	δ_y	P_u	δ_u	P_{max}	δ_{Pmax}	$\mu =$	P_{max}/P_y
(%)	(kN)	(mm)	(kN)	(mm)	(kN)	(mm)	δ_u/δ_y	
0	18.2	6.25	27	24.9	31.9	12.5	3.98	1.75
1	20.4	6.25	40.6	49.9	40.6	49.9	7.98	1.99
1.5	22.0	6.25	44.1	49.8	44.1	49.8	7.97	2.01
2	24.1	6.25	42.6	24.9	45.8	12.4	3.98	1.90
2.5	26.7	6.25	44.9	24.9	50.3	12.4	3.98	1.88

(a)

V_f	P_y	δ_y	P_u	δ_u	P_{max}	δ_{Pmax}		P_{max}/P_y
(%)	(kN)	(mm)	(kN)	(mm)	(kN)	(mm)	$\mu = \delta_u/\delta_y$	
*CJ**	18.2	6.25	27	24.9	31.9	12.5	3.98	1.75
0	15.0	6.25	28.4	12.4	28.4	12.4	1.98	1.89
1	15.8	6.25	35.5	24.8	35.5	24.8	3.97	2.25
1.5	17.6	6.25	37.1	24.8	42.7	27.6	3.97	2.62
2	19.3	6.25	50.0	49.6	45.21	24.8	7.94	2.34
2.5	22.8	6.25	47.6	24.8	47.6	24.8	3.97	2.09

(b)
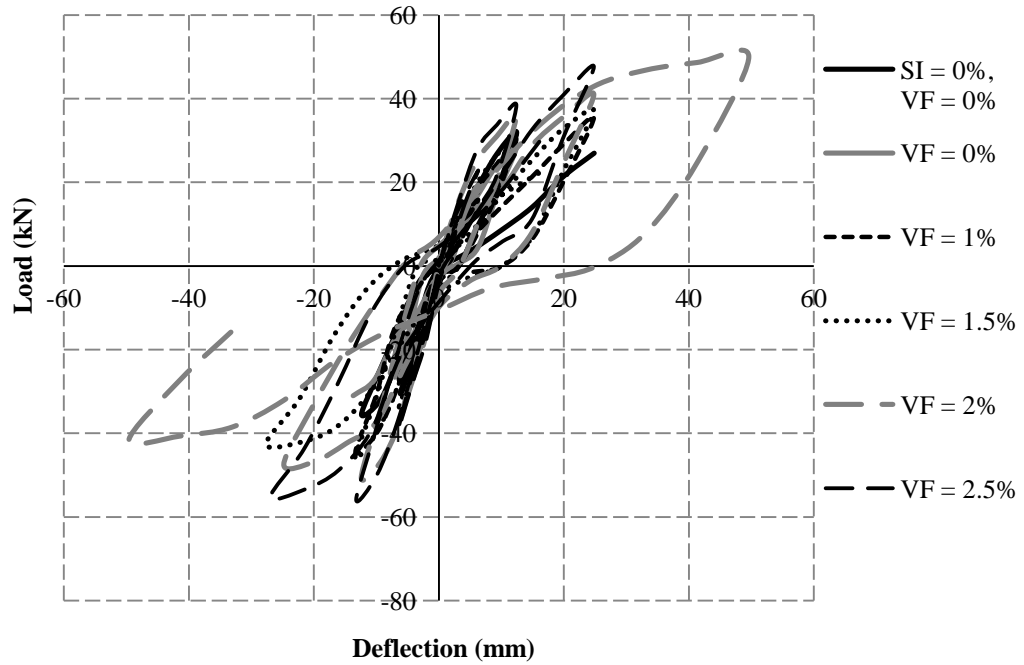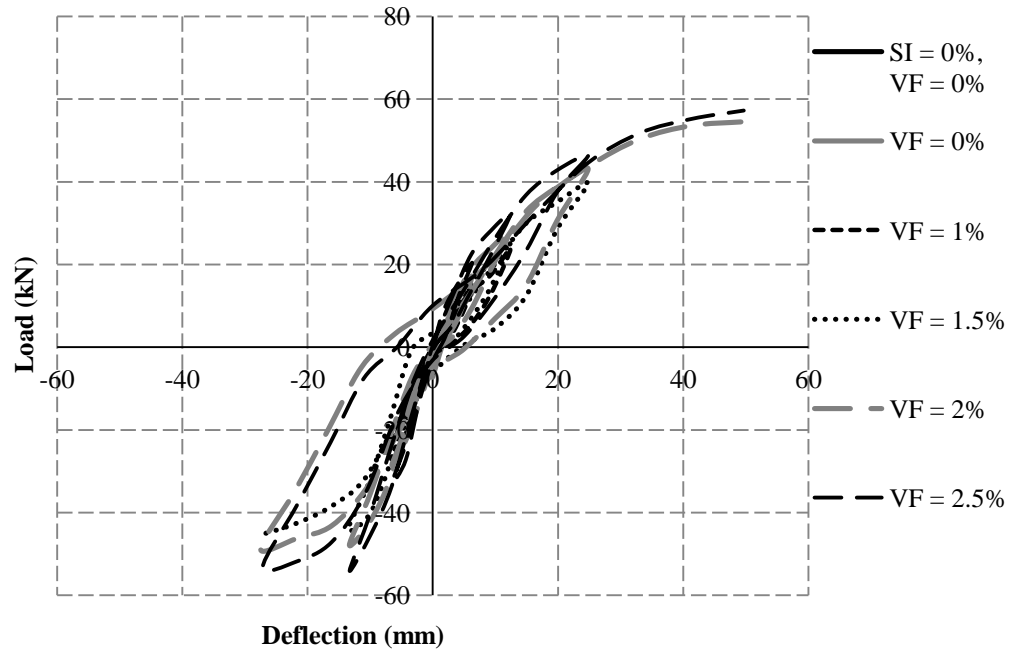
V_f (%)	P_y (kN)	δ_y (mm)	P_u (kN)	δ_u (mm)	P_{max} (kN)	δ_{Pmax} (mm)	$\mu = \delta_u/\delta_y$	P_{max}/P_y
CJ*	18.2	6.25	27.0	24.9	31.9	12.5	3.98	1.75
0	13.2	6.25	13.2	6.25	13.2	6.25	1	1
1	14.1	6.25	23.7	12.4	23.7	12.4	1.98	1.68
1.5	15.6	6.25	39.7	24.8	39.7	24.8	3.97	2.55
2	17.1	6.25	54.5	49.6	43.6	24.8	7.94	2.55
2.5	20.4	6.25	57.2	49.6	46.4	24.8	7.94	2.27

(c)

Figure 14: Load-displacement hysteresis curves obtained for the parametric studies on external joints for (a) SI = 0, (b) SI = 50% and (c) SI =100%

35
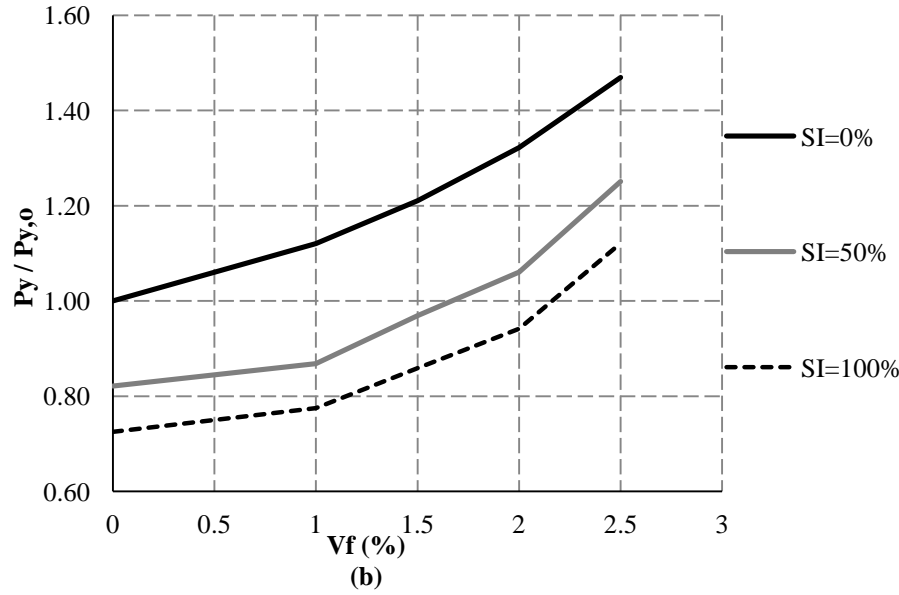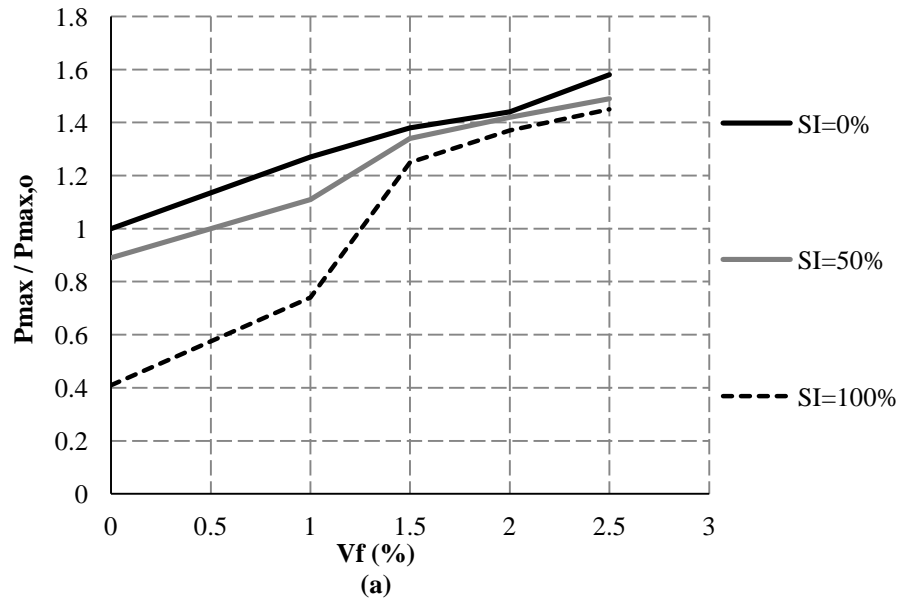
Figure 15: Variation of (a) load carrying capacity (normalized to the load carrying capacity of the control joint $P_{max,0}$) and (b) yield load (normalized to the yield load of the control joint $P_{y,0}$) for different values of V_f and SI for external joints
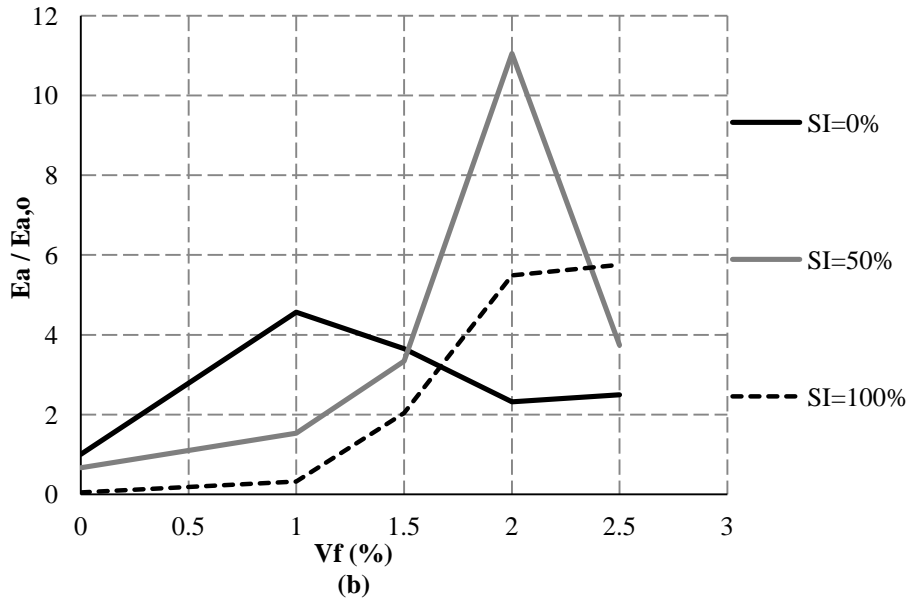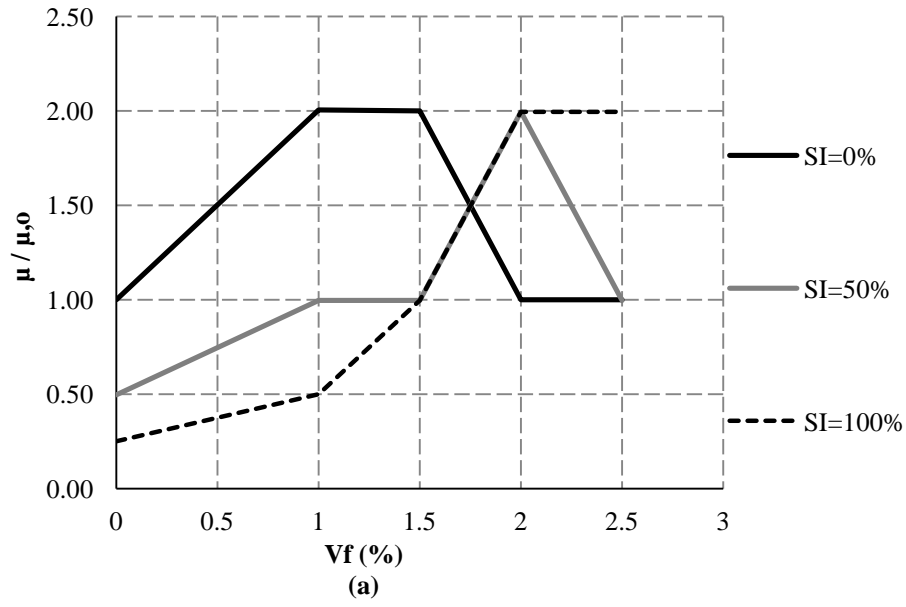
Figure 16: Variation of (a) ductility (normalized to the ductility of the control joint $\mu_{,o}$) and (b) energy absorption (normalized to the energy absorption of the control joint $E_{a,0}$) for different values of V_f and SI for external joints
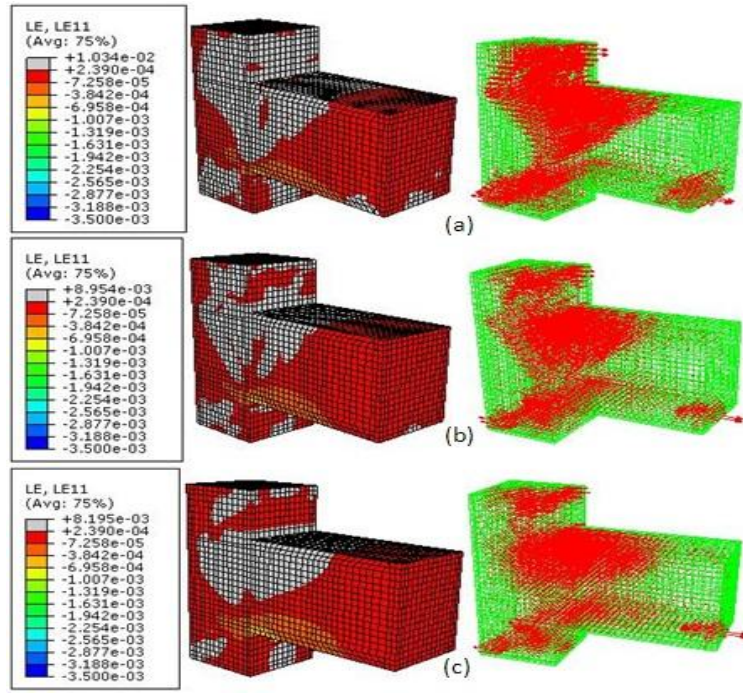
Figure 17: Principal strain contours and vectors for external joints with *SI* = 0% and (a) V_f = 0%, (b) V_f = 1%, (c) V_f = 2%; at end of first cycle (i.e. δ_y = 6.25 mm)
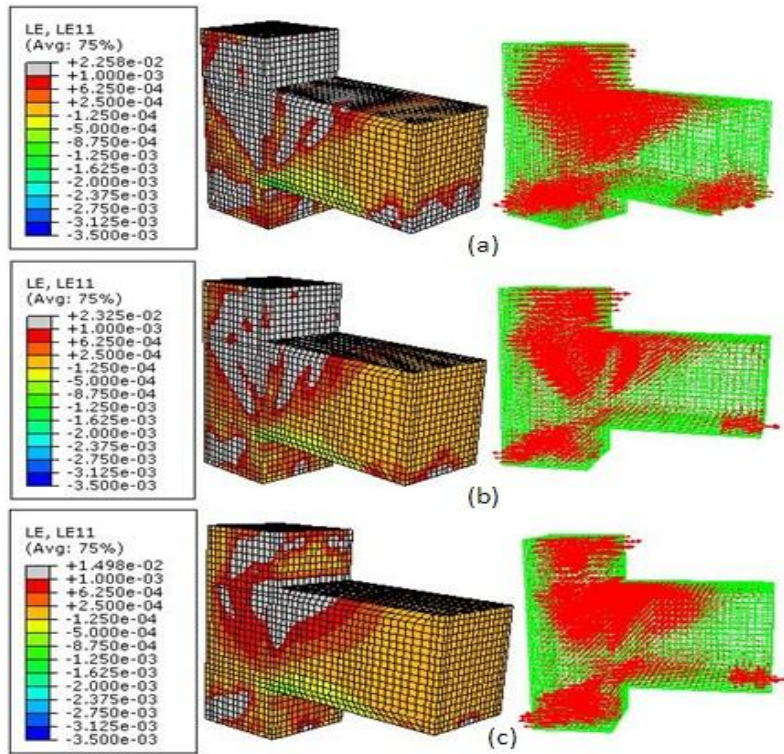
Figure 18: Principal strain contours and vectors for external joints with *SI* = 0% and (a) V_f = 0%, (b) V_f = 1%, (c) V_f = 2%; at end of second cycle (i.e. δ_2 = 12.5 mm)
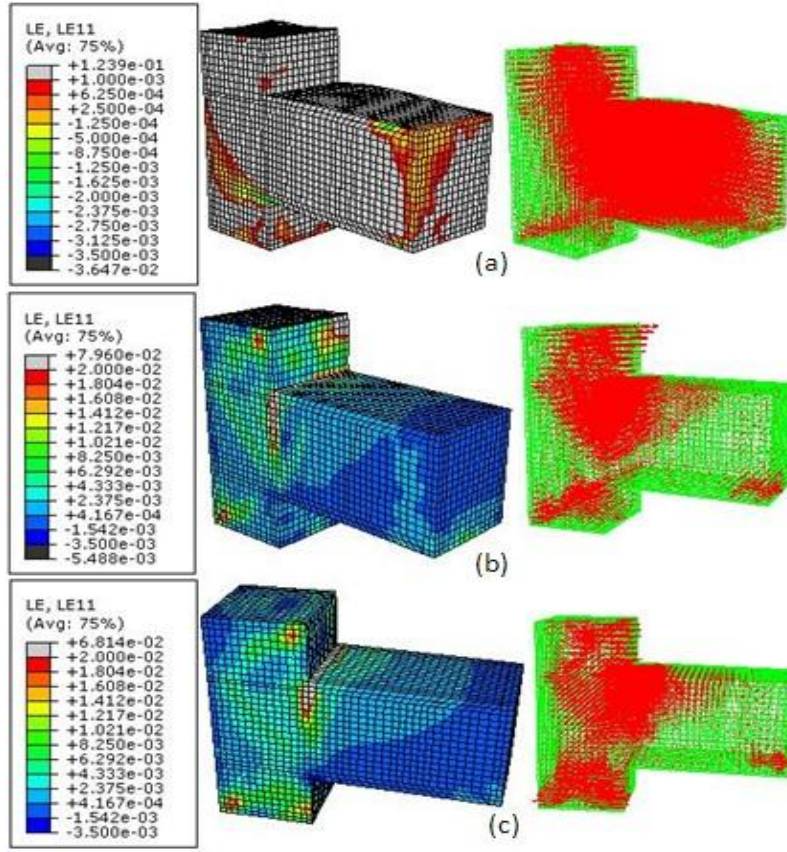
Figure 19: Principal strain contours and vectors for external joints with *SI* = 0% and (a) V_f = 0%, (b) V_f = 1%, (c) V_f = 2%; at end of third cycle (i.e. δ_3 = 24.9 mm)
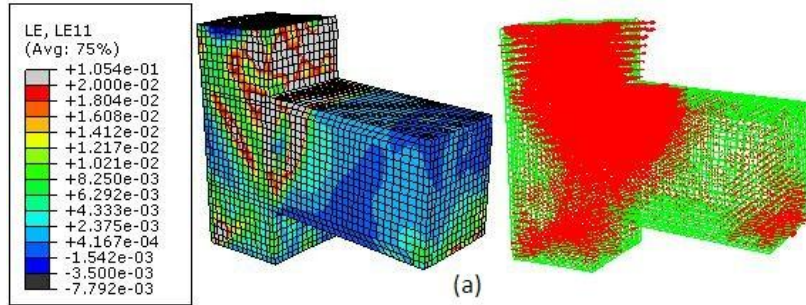
Figure 20: Principal strain contours and vectors for external joints with *SI* = 0% and V_f = 1%; at end of forth cycle (i.e. δ_4 = 49.9mm)
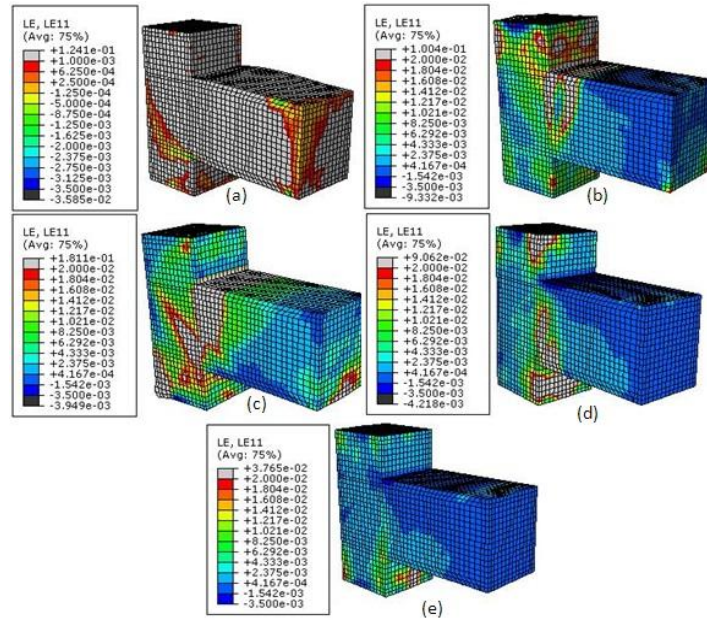
Figure 21:   Principal strain contours prior to failure for external joints with *SI* = 0% and (a) *V_f* = 0%, (b) *V_f* = 1%, (c) *V_f* = 1.5%, (d) *V_f* = 2% and (e) *V_f* = 2.5%
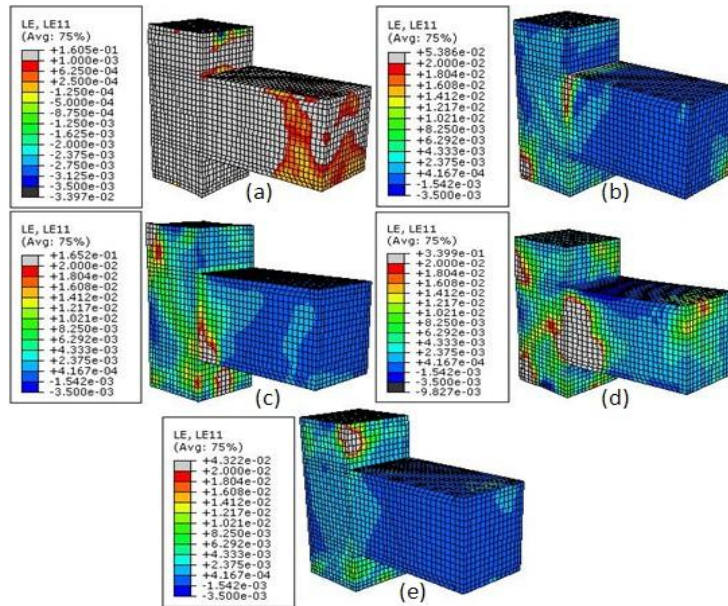
Figure 22: Principal strain contours prior to failure for external joints with *SI* = 50% and (a) *V_f* = 0%, (b) *V_f* = 1%, (c) *V_f* = 1.5%, (d) *V_f* = 2% and (e) *V_f* = 2.5%

Figure 23: Principal strain contours prior to failure for external joints with *SI* = 100% and (a) V_f = 0%, (b) V_f = 1%, (c) V_f = 1.5%, (d) V_f = 2% and (e) V_f = 2.5%
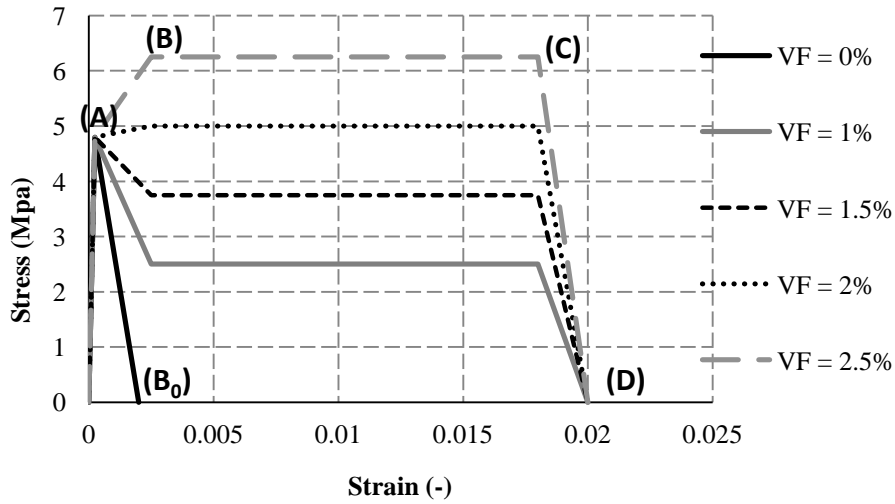
Figure 24:   Stress-strain relations in tension adopted for parametric studies on internal joints

(a)

(b)

(c)

(d)

(e)
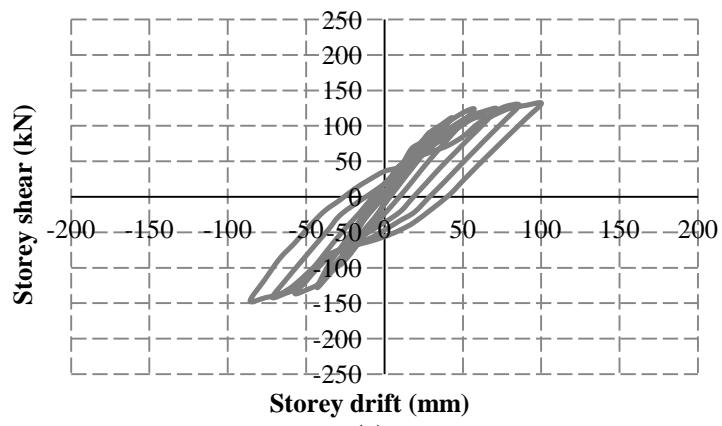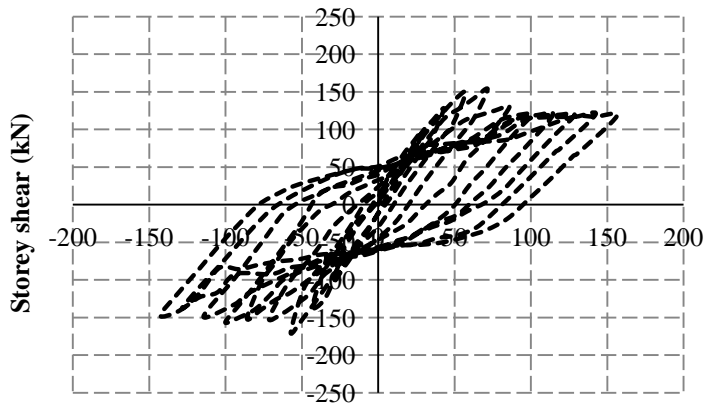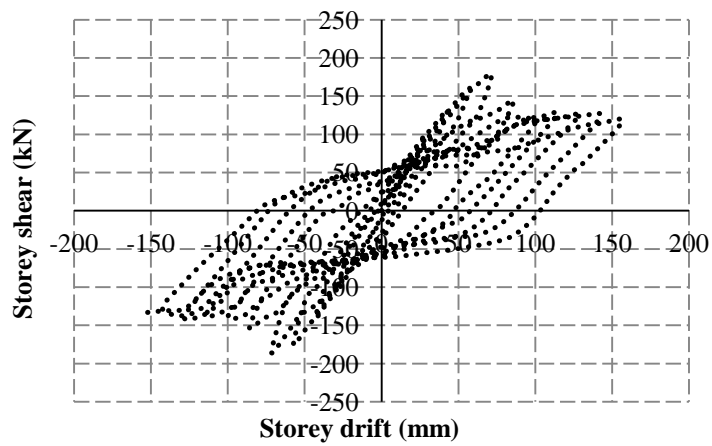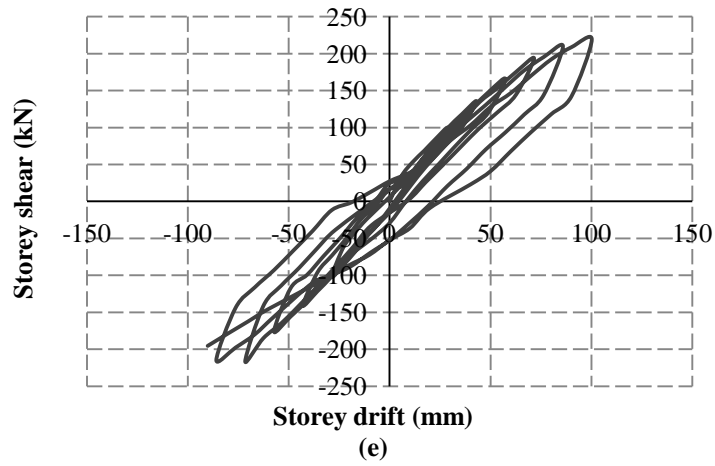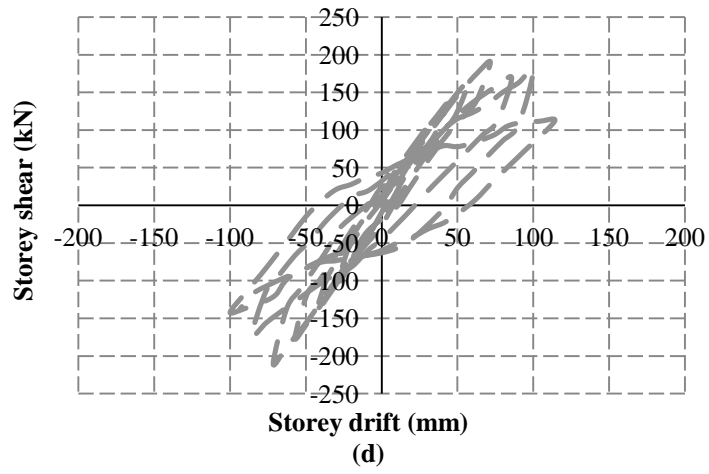
V_f (%)	V_y (kN)	$Δ_y$ (mm)	V_{max} (kN)	$Δ_{Vmax}$ (mm)	V_u (kN)	$Δ_u$ (mm)	$μ = Δ_u/Δ_y$	V_{max}/V_y
CJ	92.4	28.8	143.1	84.3	124.2	140.8	4.90	1.55
0	90.7	28.6	131.8	100	132	100.1	3.50	1.45
1	97.5	28.6	153.7	71.6	118	156.2	5.46	1.58
1.5	98.8	28.6	177.8	71.6	117	156.5	5.47	1.80
2	99.3	28.6	189.9	71.6	112	114.1	3.98	1.91
2.5	99.6	28.6	219.3	100	219	100.2	3.50	2.20

Figure 25: Storey shear-drift hysteresis curves for internal joints with single stirrups and (a) V_f = 0%, (b) V_f = 1%, (c) V_f = 1.5%, (d) V_f = 2% and (e) V_f = 2.5%

Storey shear (kN)

−200 −150 −100 −50 0 50 100 150 200

Storey drift (mm)

(a)

Storey shear (kN)

−200 −150 −100 −50 0 50 100 150 200

Storey drift (mm)

(b)

Storey shear (kN)

−200 −150 −100 −50 0 50 100 150 200

Storey drift (mm)

(c)

Storey shear (kN)

−200 −150 −100 −50 0 50 100 150 200

Storey drift (mm)

(d)

(e)
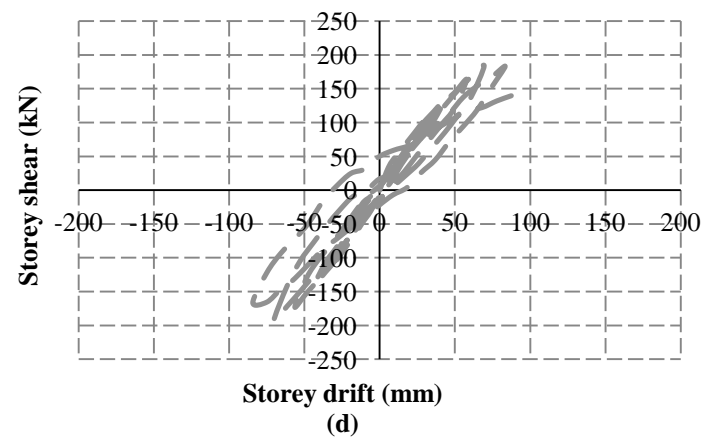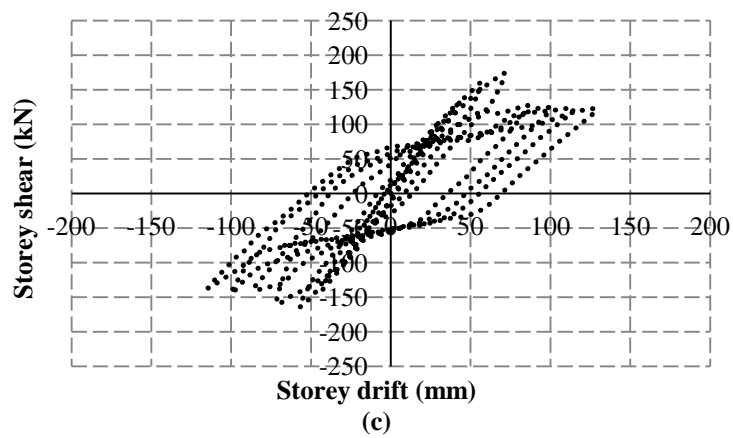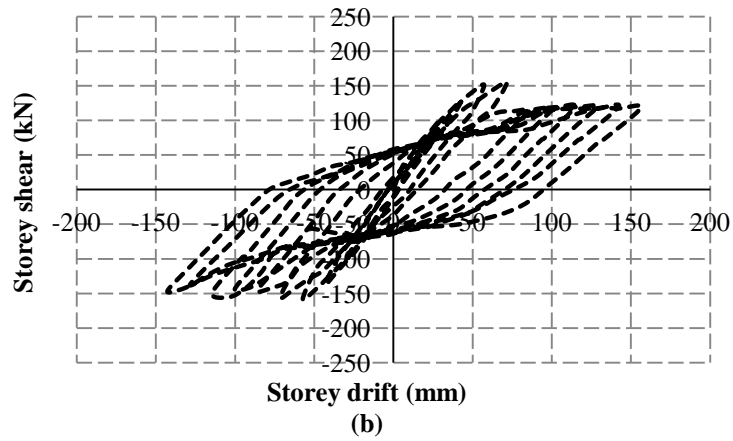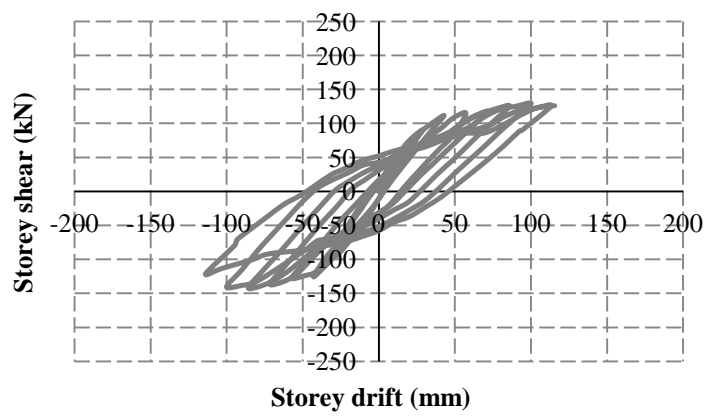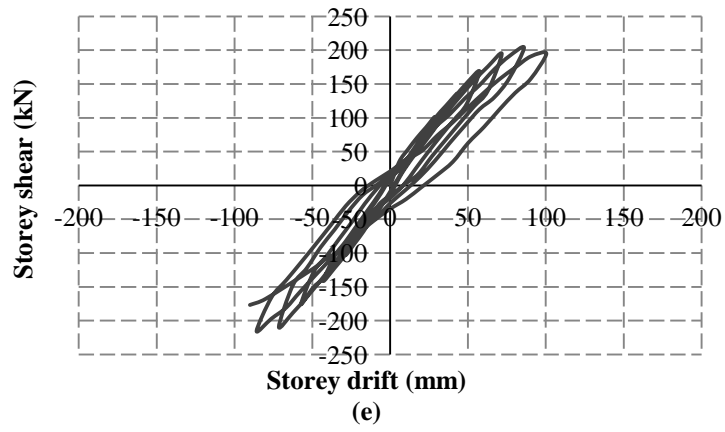
V_f (%)	V_y (kN)	Δ_y (mm)	V_{max} (kN)	Δ_{Vmax} (mm)	V_u (kN)	Δ_u (mm)	$\mu = \Delta_u/\Delta_y$	V_{max}/V_y
CJ	92.4	28.8	143.1	84.3	124.2	140.8	4.90	1.55
0	90.2	28.6	129.6	100	128	127.2	4.44	1.44
1	97.8	28.6	154.4	71.6	118	156.2	5.46	1.58
1.5	99.2	28.6	172.5	71.6	121.2	128.7	4.50	1.74
2	100	28.6	193.1	70.4	140	87.55	3.06	1.93
2.5	101	28.6	215.4	85.9	195	100.2	3.50	2.13

Figure 26: Storey shear-drift hysteresis curves for internal joints with Sl = 50% and (a) V_f = 0%, (b) V_f = 1%, (c) V_f = 1.5%, (d) V_f = 2% and (e) V_f = 2.5%

(a)



(b)

(c)

(d)

(e)
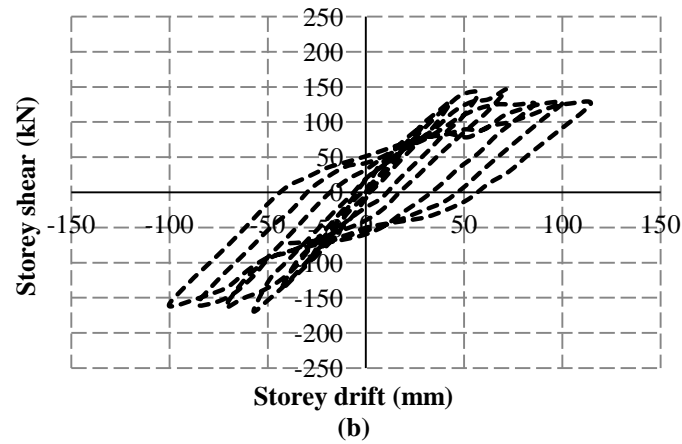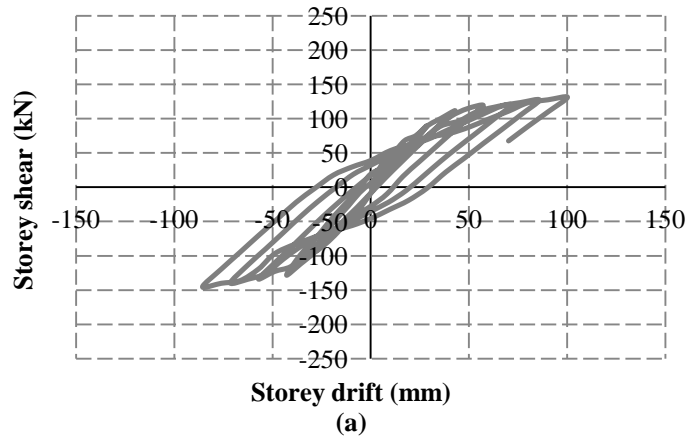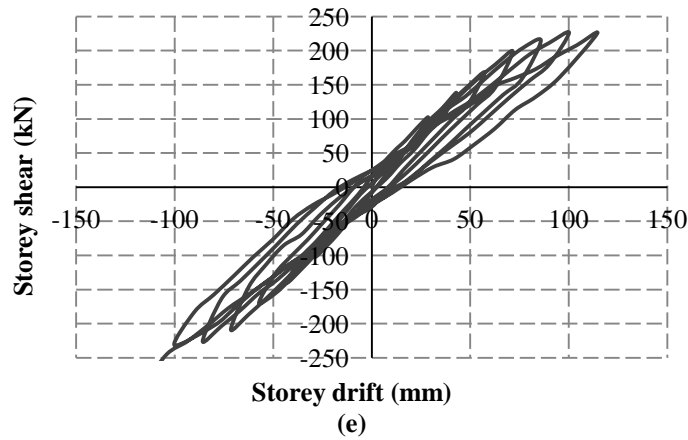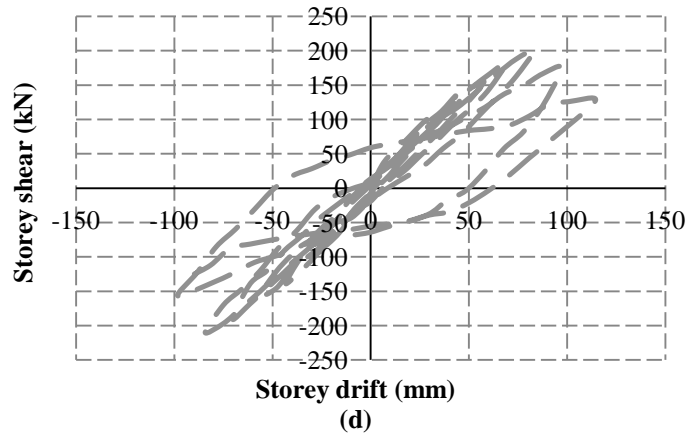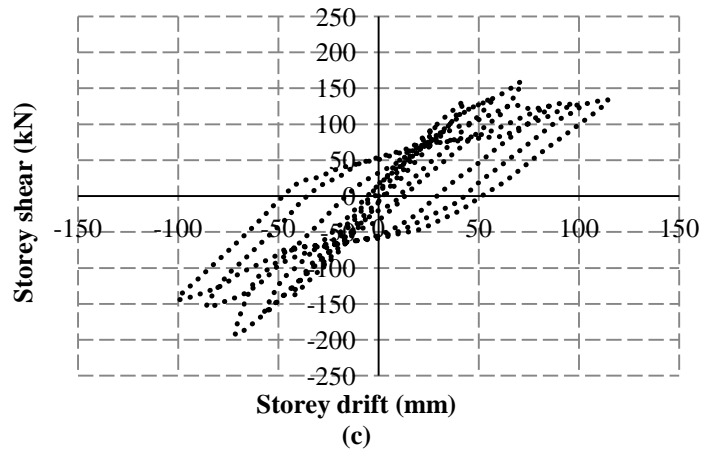
V_f	V_y	$Δ_y$	V_{max}	$Δ_{Vmax}$	V_u	$Δ_u$		$V_{max}/$
(%)	(kN)	(mm)	(kN)	(mm)	(kN)	(mm)	$μ = Δ_u/Δ_y$	V_y
CJ	92.4	28.8	143.1	84.3	124.2	140.8	4.90	1.55
0	89.9	28.6	131.2	100	131	100.1	3.50	1.46
1	93.6	28.6	146.1	71.6	132	114.2	4.00	1.56
1.5	96.5	28.1	158.3	71.6	132	114.4	4.07	1.64
2	98.53	28.1	187.8	73.9	128	114.4	4.07	1.91
2.5	99.25	27.5	214.9	85.9	225.3	114.5	4.16	2.13

Figure 27: Storey shear-drift hysteresis curves for internal joints with *SI* = 100% and (a) V_f = 0%, (b) V_f = 1%, (c) V_f = 1.5%, (d) V_f = 2% and (e) V_f = 2.5%
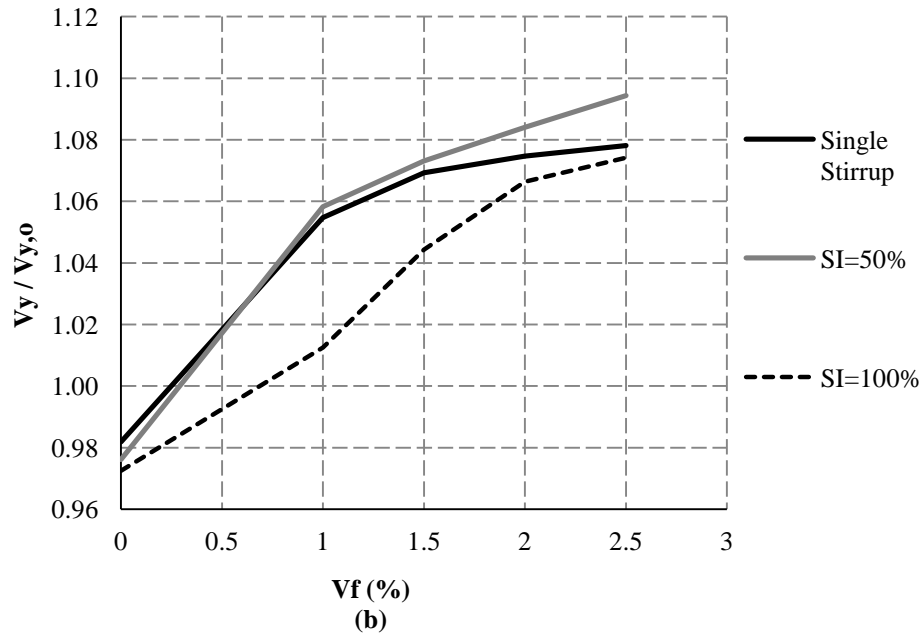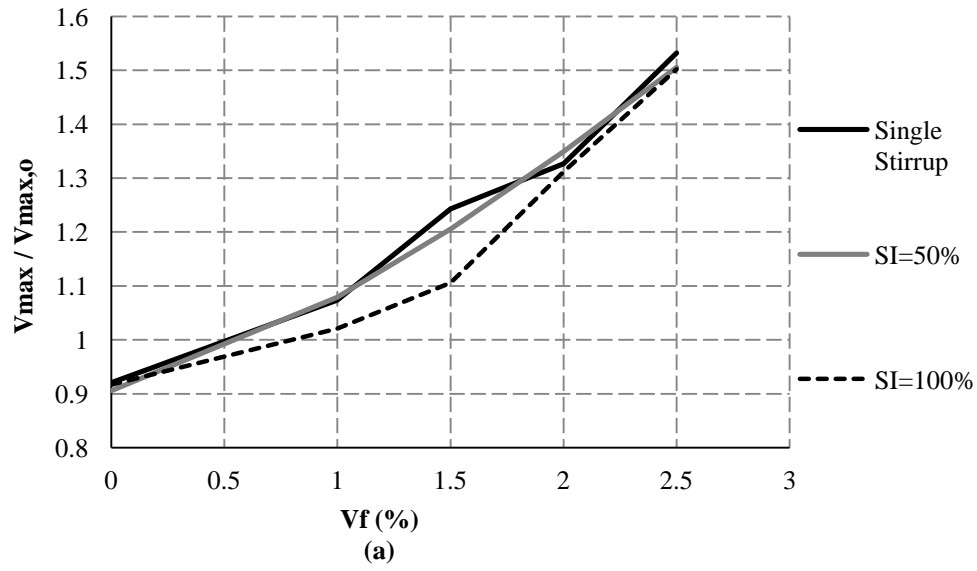
Figure 28: Variation of storey-shear associated with (a) load carrying capacity and (b) load at yield (both normalized to control specimen corresponding vales) for different values of V_f and SI for internal joints
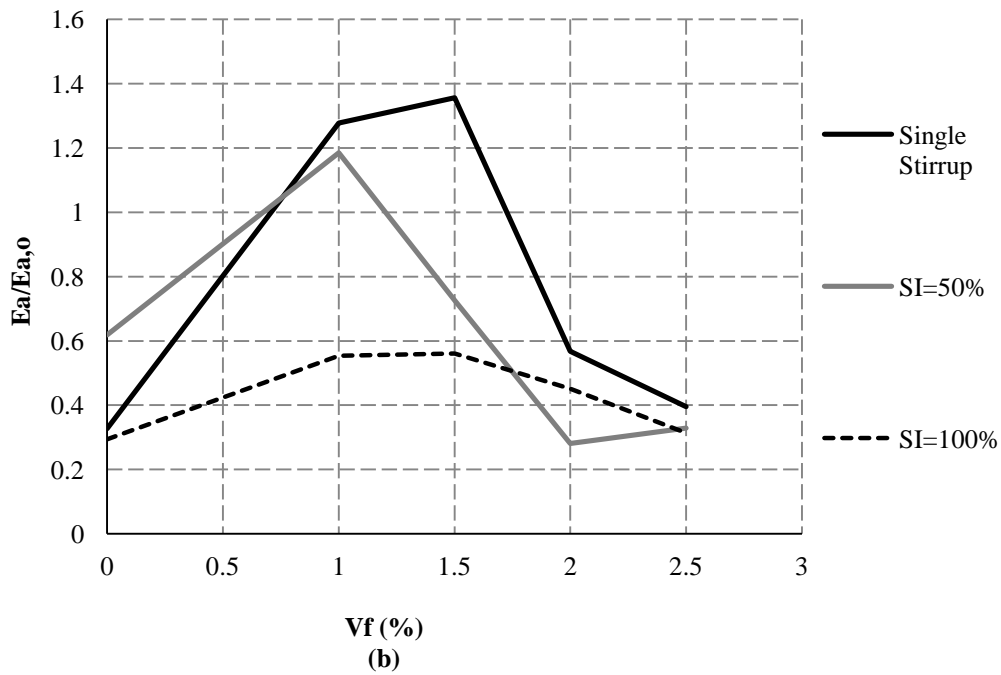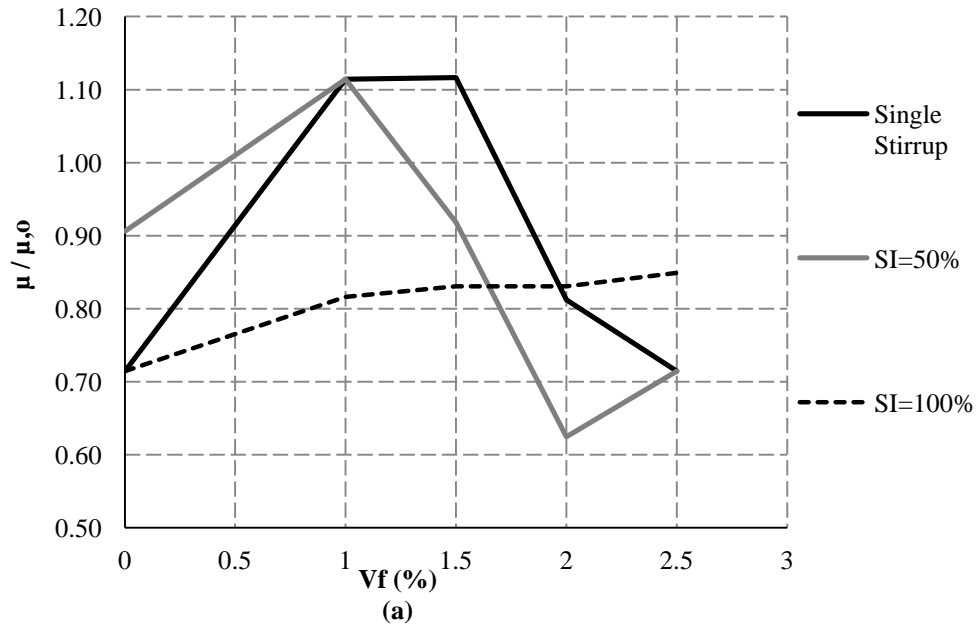
Figure 29: Variation of (a) ductility ratio and (b) energy absorption (both normalized to control specimen corresponding vales) for different values of V_f and SI for internal joints
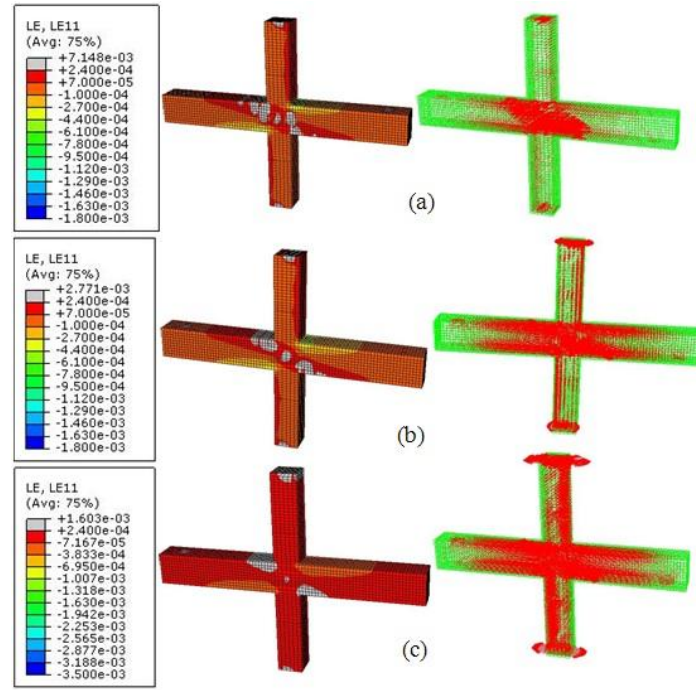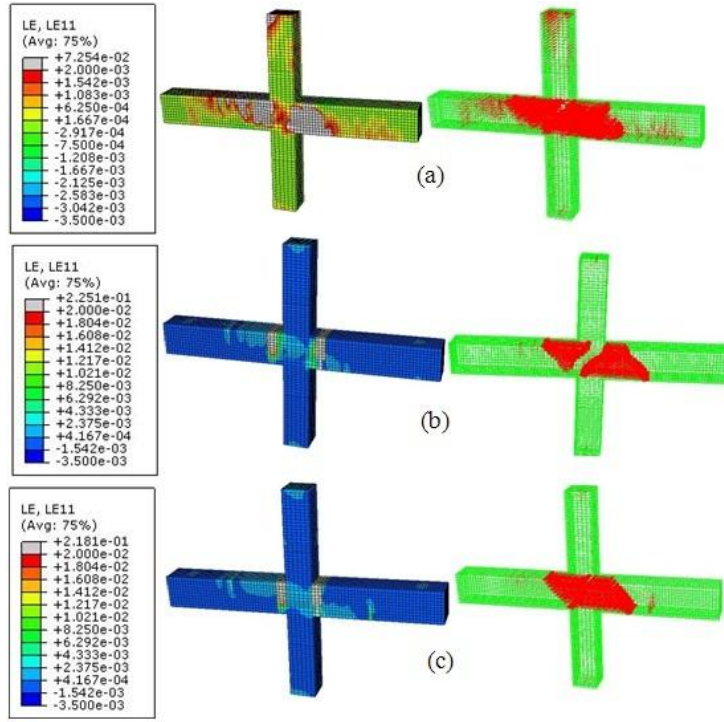
Figure 30: Principal strain contour and vectors for internal joints with *SI* = 50% and (a) V_f = 0%, (b) V_f = 1%, (c) V_f = 2% taken from storey drift at $Δ_y$ = 28.6mm
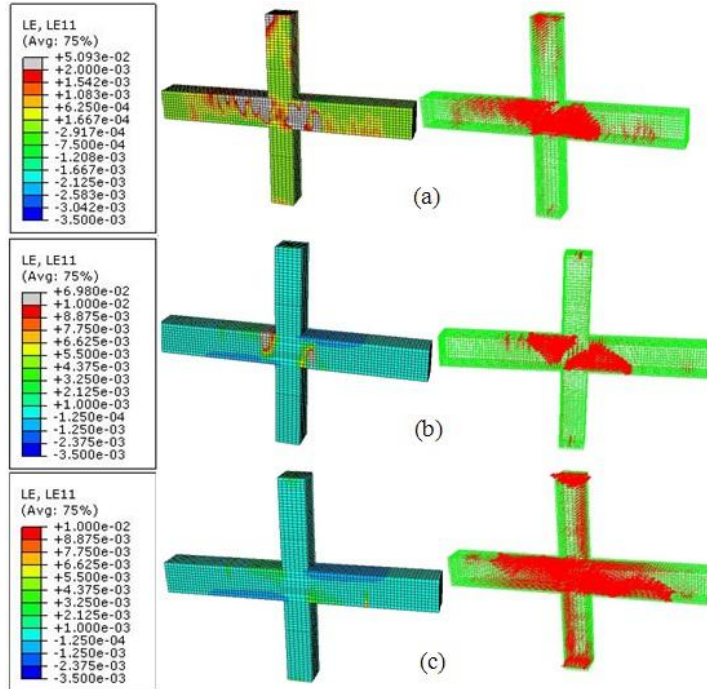
Figure 31: Principal strain contour and vectors for internal joints with *SI* = 50% and (a) V_f = 0%, (b) V_f = 1%, (c) V_f = 2% taken at $Δ_{max}$ = 69.4mm
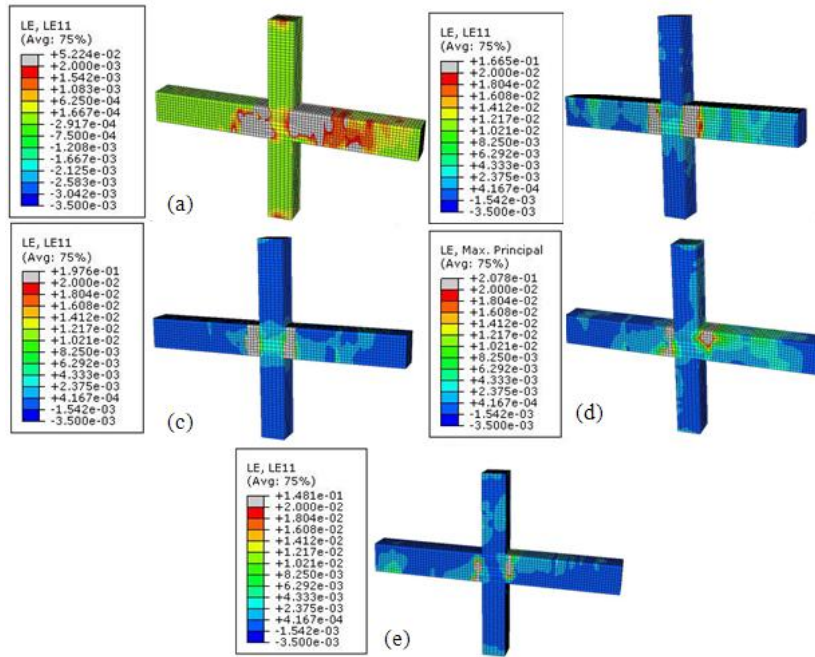
Figure 32: Principal strain contours and vectors for internal joints with *SI* = 50% and (a) *V_f* = 0%, (b) *V_f* = 1%, (c) *V_f* = 2% taken at *Δ*_u = 100.2mm

Figure 33: Principal strain contours for internal joints with single stirrups and (a) *V_f* = 0%, (b) *V_f* = 1%, (c) *V_f* = 1.5%, (d) *V_f* = 2% and (e) *V_f* = 2.5%
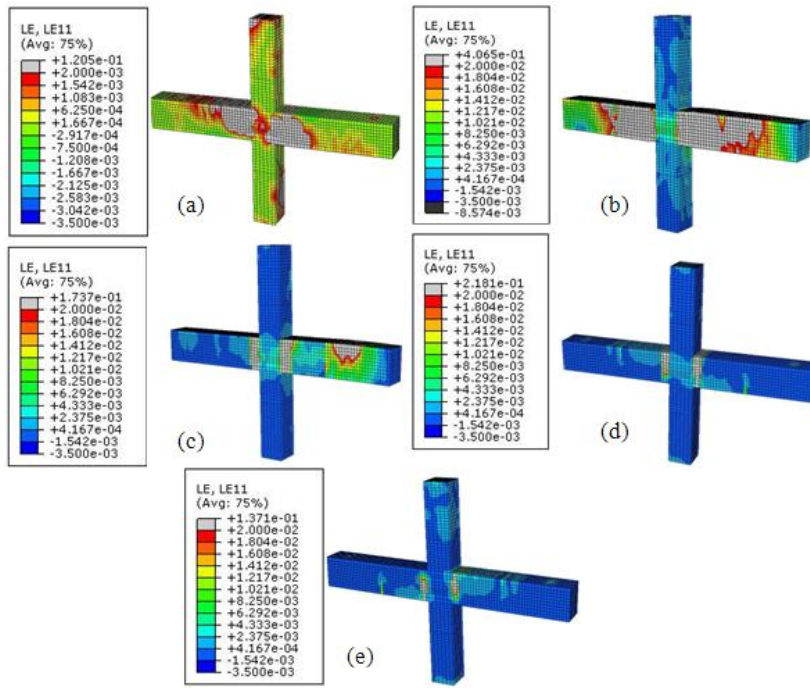
Figure 34: Principal strain contours for internal joints with SI = 50% and (a) V_f = 0%, (b) V_f = 1%, (c) V_f = 1.5%, (d) V_f = 2% and (e) V_f = 2.5%
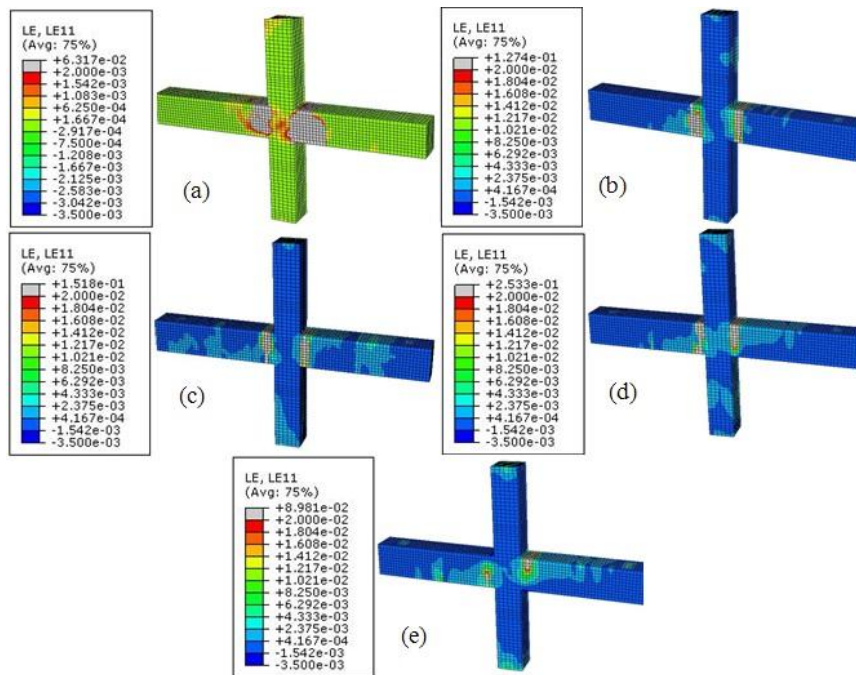

Figure 35: Principal strain contours for internal joints with SI = 100% and (a) V_f = 0%, (b) V_f = 1%, (c) V_f = 1.5%, (d) V_f = 2% and (e) V_f = 2.5%
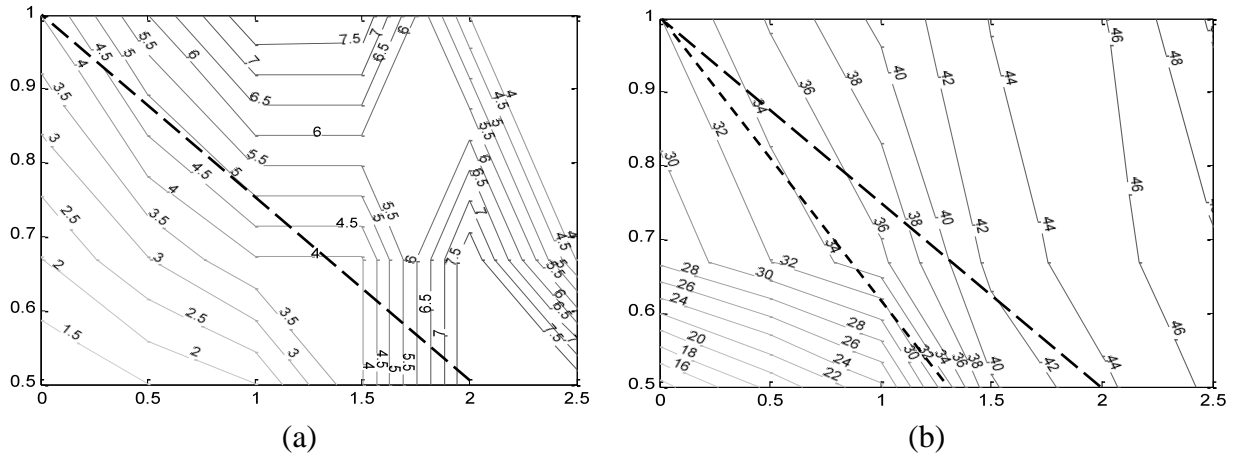
Figure 36: Contours showing the variation of (a) ductility ratio μ and (b) load-carrying capacity P_{max} for different values of r_{sw} and V_f for external joints